UNIVERSITÀ DEGLI STUDI DI MILANO &
UNIVERSITÀ CATTOLICA DEL SACRO CUORE

SCUOLA DI DOTTORATO IN
FISICA, ASTROFISICA E FISICA APPLICATA

DIPARTIMENTO
MATEMATICA E FISICA

DOTTORATO DI RICERCA IN
FISICA, ASTROFISICA E FISICA APPLICATA
Ciclo XXVI

Dynamic Atomic Force Microscopy resolved by wavelet transform

Settore scientifico disciplinare FIS/03

Tesi di Dottorato di:
Valentina Pukhova

Coordinatore: Prof. Marco Bersanelli
Tutore: Prof. Gabriele Ferrini

A. A. 2014-2015

To my family

Contents

List of Figures

List of Tables

Introduction

Motivation

Atomic Force Microscopy (AFM) [1] is perhaps the most significant member of the scanning probe microscopes family and, because of its capability of working in air and liquid environments with virtually no limitations on imaging conditions and types of samples, it is definitely one of the most widely used. It has become an indispensable tool to measure mechanical properties at the nanoscale in various research contexts.

Scanning probes used in AFM are micromechanical oscillators (typically cantilevers) and the theory of AFM dynamics is based on the analysis of the oscillating modes of beam resonators or the simpler spring-mass model [2, 3]. Cantilevers can be driven by the thermal excitation [4–8] and/or an external driver [2, 3]. Usually cantilevers are driven near resonances corresponding to flexural eigenmodes that can be described as damped harmonic oscillators [9]. Advanced techniques consider multifrequency excitation [10, 11] or band excitation [12, 13] to broaden the measurable events in tip-sample interactions, thus expanding the variety of sample properties that can be accessed.

Multifrequency methods imply excitation and/or detection of several frequencies of the cantilever oscillations and concern the associated nonlinear cantilever dynamics [10,14–25]. Such excitation/detection schemes provide higher resolution and sensitivity to materials properties such as the elastic constants and the sample chemical environment with lateral resolution in the nanometer range. In order to measure these parameters, information on peak force of interaction, energy dissipation and contact

dynamics is required. Techniques to measure the parameters of the cantilever in the stationary regime are well established [26, 27]. In dynamics methods the external driver (thermal noise, piezoelectric driver, etc.) excites the cantilever and a number of techniques have been implemented to gain information from the tip-sample interactions, but usually the interaction of the tip with the surface is revealed by the modification of the average value of the amplitude, frequency or phase shift over many oscillation cycles [28, 29]. Reconstruction of the complete evolution of the interaction force between the tip and the sample surface during a single interaction event is not even considered [2, 3].

As an alternative to these well established techniques and to push further the AFM possibilities, it is important to examine the possibility of analyzing single-event or impulsive interactions. This opens the possibility to capture the information conveyed by the sensing tip in a single interaction, in contrast to the cycle average used in many dynamic techniques. The single-event interactions are basically of the impact kind, with the simultaneous excitation of many cantilever eigenmodes and/or harmonics. The averaging techniques provide superior sensibility, allowing to probe the details of force interactions down to the molecular level [2, 28, 30, 31], but to study single-event interactions it is mandatory to provide analysis techniques that are able to characterize all excited cantilever oscillation modes at once without averaging. The temporal evolution of the amplitude, phase and frequency during few oscillation cycles of the cantilever provides information that cannot be obtained with standard methods. In the present thesis a data analysis method allowing to retrieve these quantities during an impulsive cantilever excitation is proposed.

This thesis concentrates on the dynamics of the flexural modes of the thermally driven cantilever in air when its tip is excited by a single impact on the sample surface. The signal analysis is based on the combination of wavelet and Fourier transforms that can be applied to a broad class of AFM impulsive measurements. To exemplify the method, a short time interval around the jump-to-contact (JTC) transition in ambient conditions is investigated, with the aim to characterize the transient excitation of the cantilever eigenmodes before and after the impact. The experimental evidences that high-order flexural modes are excited in air upon a single impact tip–sample interaction induced by the JTC transition are presented. The way to retrieve information about the instantaneous total force act-

ing on the cantilever tip, contact dynamics and energy dissipation at all frequencies simultaneously, without averaging or interruption, is developed. The exploration of these transient conditions of the cantilever is not possible with dynamic techniques based on the resonant driving or using Fourier transform analysis alone.

The analysis presented in this work is useful to deal with non-repeatable experiments and to determine the exact single interaction dynamics in terms of the full cantilever spectral excitations, features that are not normally considered in dynamical AFM techniques.

Thesis overview

The thesis consists of two Parts, for a total of five Chapters. Part I is constituted of Chapters 1 and 2 and is dedicated to introductory remarks about the development of the techniques and the methods of analysis. Part II is composed of Chapters 3, 4 and 5 and is devoted to the experimental results. These chapters are adapted version of the articles [32–34] which have been published before in various scientific journals. The previously published results have been modified to maintain the consistency in style and structure.

- Chapter 1: Emergence of multifrequency Atomic Force Microscopy. In this chapter a brief review of the recent developments of dynamic atomic force microscopy is presented.

- Chapter 2: Data analysis in Atomic Force Microscopy by Fourier and wavelet transforms. This chapter is devoted to the description of the methods of data analysis. The Fourier transform (FT) and the wavelet transform (WT) analysis are introduced. The main drawback of FT with comparison to WT in studying transitory regimes (signals with a frequency spectrum rapidly changing during the time) is discussed.

- Chapter 3: Experiment. In this chapter the experimental set-up, samples and experimental conditions are described.

- Chapter 4: Complex eigenmodes dynamics of the interacting cantilever resolved by wavelet transform. In this chapter the cantilever dynamics in time and frequency is described. It is shown that WT

allows characterizing the instantaneous time-frequency response of the cantilever parameters during the tip-sample interaction. As an example, the force spectroscopy curve of the thermally driven cantilever in ambient conditions as it approaches the sample surface is analyzed. The measure of the instantaneous cantilever frequency shift carries information about the interaction of the tip with the surface forces. The response of the cantilever is revealed starting from the very beginning of the tip interaction with the surface across the jump-to-contact transition and beyond. At the moment of the jump-to-contact the excitation of the higher flexural modes is revealed. The analysis for different types of materials is presented and the advantages of wavelet transform in comparison with the Fourier transform are discussed. This chapter is the adapted version of a work submitted for publication [32].

- Chapter 5: Wavelet transform analysis of single-impact cantilever dynamics. This chapter is dedicated to demonstrate that the information already present in a standard force curve can be exploited to reconstruct the tip trajectory immediately after the jump-to-contact impact and to access the dissipated energy per cycle in each mode. The tip trajectory reconstruction naturally stems from the wavelet analysis and is not the result of the fitting procedure. The instantaneous displacement, velocity, acceleration and total force acting on the cantilever tip during the single impact are reconstructed. This chapter is the adapted version of the previously published articles [33, 34].

Part I

Introductory remarks

CHAPTER 1

Emergence of multifrequency Atomic Force Microscopy

1.1 Dynamic Atomic Force Microscopy

Since its invention [1] AFM is considered as a key instrument in material science and plays an important role in the development of nanotechnology. In its first operating mode, the static mode, the deflection of a cantilever is measured during the scanning across the sample surface while the cantilever tip stays in the mechanical contact with the surface [26,27]. The static mode has been superseded by dynamic AFM methods [28,29,35–38].

In dynamic AFM the cantilever is excited at its first resonant eigenmode (or very close to it) while scanning the sample surface. The excitation is performed in the vertical direction, so the flexural mode is excited. Three dynamic AFM methods have been implemented: amplitude modulation AFM (AM-AFM) [2,3,35], frequency modulation AFM (FM-AFM) [28,38,39] and phase modulation AFM (PM-AFM) [37,38,40]. They can be distinguished according to the cantilever excitation and force detection methods, or in other words, according to the parameter that is used to maintain the feedback loop [28,38].

With respect to static (contact) AFM mode, dynamic methods offer important advantages. First, soft materials can be imaged without damage, since dynamic techniques operate at smaller forces. Second, dynamic AFM has high spatial resolution: atomic resolution has been demonstrated in liquids and vacuum [41,42]. Third, in dynamic AFM the tip-sample interactions may be sensed not only by the cantilever deflection but by several parameters: oscillation amplitude, frequency or phase

shift. All these data may be acquired simultaneously to characterize different material properties at the nanoscale.

The invention of dynamic AFM methods stimulated an intense application of AFM in biology and medicine and allowed to study a variety of soft materials, such as polymers, cells, proteins and DNA [43–45] with high resolution in different environments [37, 42, 46, 47] that led to a renaissance in nanomechanics.

1.2 Multifrequency Atomic Force Microscopy

The goal of any dynamic AFM experiment is to gain information about the properties of the sample surface encoded in the dynamics of the cantilever. Conventional dynamic atomic force microscopy methods (see section 1.1) consider the excitation and detection of the first resonance frequency of the cantilever. However, the dynamic of the cantilever could be highly nonlinear and characterized by the presence of higher harmonics and eigenmodes in the recorded signal as an integral part of the cantilever motion. In conventional dynamic AFM information contained in the higher frequency components is irrevocably lost.

This led to the invention of the multifrequency excitation and detection schemes [10, 12, 14–16, 21, 44, 48–52]. Multifrequency atomic force microscopy implies the excitation and/or detection of several frequencies of the cantilever oscillations [10]. Such frequencies are associated with either the higher harmonics of the oscillation frequency or the eigenmodes of the cantilever.

Multifrequency excitation/detection methods are particularly designed to gain the information produced by the nonlinear regions of the tip-sample interaction force [10]. They provide spatial resolution and sensitivity higher than those of the conventional dynamic techniques. At the present time, multifrequency AFM has already offered a number of applications in biology and medicine including the mapping of the protein flexibility and ion diffusion, imaging of the subsurfaces of biological specimens and investigation of the energy storage [18, 20, 53–55].

1.2.1 Theory of Multifrequency Atomic Force Microscopy

In conventional dynamic AFM methods the excitation and detection of the cantilever oscillations are performed at a single frequency. While

the tip is interacting with the surface, higher frequency components in the cantilever dynamics arise caused by the nonlinearities in the interaction force. These components carry information about the sample properties. The existence of these additional components in the detected signal has been known for several years but their role in the cantilever dynamic, spatial resolution and sensitivity to material properties was not appreciated.

The oscillations of the non-interacting cantilever are purely sinusoidal: $A\cos(\omega t)$, where ω is the driving frequency and A is the initial amplitude of the oscillations. The contribution of the components that contains higher harmonics in the cantilever motion can be described as $\sum_{n=1}^{\infty} a_n \cos(n\omega t + \varphi_n)$, where a_n is the amplitude (note that it decreases as $1/n^2$) and φ_n is the phase shift of the n-harmonic, n is an integer number.

Worth to notice, the higher harmonics should be distinguished from the higher modes of the cantilever. The higher harmonics are consecutive integer multiples of the fundamental cantilever resonance. The higher eigenfrequencies of the oscillating beam, however, do not form a series of consecutive integer multiples [4]. As an example, for rectangular cantilever the frequency of the second eigenmode ($6.27f$) is close to the sixth harmonic ($6f$). The values of the frequencies of the higher harmonics are close to that of the flexural eigenmodes of the cantilever. This leads to the fact that the higher harmonics act as driving forces and excite the oscillations of the higher eigenmodes of the cantilever. The higher modes contribute to the motion of the cantilever as $\sum_{i=1}^{\infty} b_i \cos(\omega_i t + \psi_i)$, where b_i is the amplitude and ψ_i is the phase shift of the i-eigenmode, i is an integer number [11].

Usually the higher frequency components were observed when large tip-surface forces were acting and large oscillation amplitudes were applied. The amplitude of these components are few orders of magnitude smaller than those of the fundamental frequency [11, 56, 57]. In these circumstances, to detect those components the signal-to-noise ratio need to be increased. Last but not least to decode the information from the frequency components in terms of sample properties an appropriate theory should be developed.

Some approaches of multifrequency AFM are reported below.

1.2.2 Higher-harmonics and higher-modes Atomic Force Microscopy

To enhance the sensitivity to the tip-sample interactions, the response of the higher harmonics [18, 19, 53, 58, 59] or the higher modes [14, 18, 54, 60–62] of the cantilever need to be considered.

When the tip of the excited cantilever comes in close vicinity of the sample surface it starts experiencing distortions because of forces acting on the tip and this leads to the excitation of higher harmonics [10, 63, 64]. Such distortions modify both the amplitude and phase of the oscillating cantilever. Thus the frequency spectrum of the higher harmonics contains detailed information on the nonlinearities of the tip-sample interaction forces [25, 59, 65, 66]. In general, the higher harmonics provide enhanced lateral resolution due to the fact that the frequency shift due to the tip-sample interaction is amplified by a factor of n for the n-th harmonic [59, 67]. The higher harmonics amplitudes are not influenced by the surface topography, but by the borders of patterns where the geometry of the tip-sample contact varies. Because of this, the excited higher harmonics provide high sensitivity to surface roughness [59]. In case of heterogeneous samples the amplitudes of the higher harmonics change with respect to the mechanical properties of the regions [59]. They can also be used to probe the elastic properties and dissipative forces [68, 69] and to perform the compositional mapping in air [23] and liquid environments [17, 19, 70, 71].

The eigenmodes of the cantilever are orthogonal to each other when the nonlinear tip-sample forces are absent. It means that the eigenmodes dynamics are independent [64]. When the tip is close to the surface and is influenced by the nonlinear surface interaction forces, higher harmonics are excited. These higher harmonics are able to excite the higher modes of the cantilever that are close to the integer multiples of the fundamental mode (see section 1.2.1). This nonlinear modal interaction is called internal resonance [20, 58, 59, 64, 72, 73]. The variations in the oscillating parameters of the higher eigenmodes are very sensitive to changes in the tip-sample interaction forces, consequently increasing the sensitivity to the mechanical [14, 24, 51], magnetic [53, 74, 75] or electric tip-sample interactions [49, 76].

1.2.3 Band excitation Atomic Force Microscopy

Understanding of the energy transformation and dissipation mechanisms in the nonlinear cantilever dynamic is an important task in the field of AFM. At the macroscale it is possible to estimate the energy dissipation in materials by means of direct measurements. The extension of these measurements at the nanoscale is a challenge. AFM methods are established to measure the surface topography and forces at the nanoscale, and it also allows studying the local dissipation processes at the same level [12,29,77,78]. In these cases, the probe is considered as a sensor for the energy dissipation. To get information about the energy dissipation due to the tip-sample interaction the dynamic of the oscillating cantilever need to be analyzed by recording variations of the amplitude and phase over a band of frequencies throughout the resonance.

In conventional dynamic AFM the cantilever excitation takes place at a single frequency, instead in BE method [10,12,13,55] an adaptive, digitally synthesized signal is used to drive the cantilever over a broad band of frequencies. The frequency region is selected to cover only the Fourier space that contains information of interest and usually the center of the frequency band coincides with the resonance frequency of the cantilever. The amplitude and phase content are established in advance in the frequency band. The response of the cantilever to the band excitation signal is acquired by a high speed data acquisition method during the scanning process. The stored data is Fourier transformed and the amplitude-frequency and phase-frequency curves are filed in multidimensional data array for ensuing analysis. This allows to collect the full spectral response in significantly reduced time [12,55].

The transfer function (full frequency response at each point) of the system within the defined band of frequencies is obtained by the ratio of the Fourier transform of the response and driving signals. Thus in BE the cantilever driving and response signals are collected over a frequency band simultaneously (parallel detection) and these data provide the essential parameters of the tip-sample interaction.

BE method can be applied to AFM working in ambient air and liquid providing direct and rapid measurements of the local energy dissipation processes at the nanoscale. This opens a way to understand the atomistic mechanism of dissipation and to explain relationships between the en-

ergy dissipation and the material structure. The method has been already successfully applied to study the electromechanical coupling in biological systems and to examine the ion diffusion in Lithium-ion batteries at the nanoscale [10,55].

1.2.4 Thermal excitation Atomic Force Microscopy

The thermal fluctuations of the cantilever due to the Brownian motion are referred to as thermal or mechanical noise [4,7,8,76,79,80]. The thermal vibrations result in positional fluctuations of the cantilever and are a fundamental and unavoidable source of noise in AFM that set the lower resolution limit [4,7,81–83].

The Brownian motion of the cantilever placed in ambient air far from the surface and subjected to the thermal excitation is described by the Langevin equation [9,84,85]

$$m\ddot{z}(t) = -\gamma\dot{z}(t) - k_0 z(t) + R(t) \tag{1.1}$$

where m is the cantilever effective mass, z is the vertical coordinate (displacement), γ is the damping coefficient, k_0 is the static spring constant and the dot $\cdot$ is the temporal derivative. The force acting on the cantilever is a sum of the drag force according to the Stokes' law $-\gamma_0\dot{z}(t)$, restoring force according to the Hooke's law $-k_0 z(t)$ and the thermal excitation random force $R(t)$.

The force $R(t)$ has a Gaussian probability distribution, hence the correlation function is defined by the Langevin hypothesis [86,87] as

$$< R(t)R(t') >= 2\gamma_0 k_B T\delta(t - t') \tag{1.2}$$

where k_B is the Boltzmann constant, T is the absolute temperature and $\delta(t - t')$ is the Dirac delta function. The delta function form of the correlations specifies that the driving force is uncorrelated in time, thus this stochastic force does not depend on frequency. The thermal noise is a white noise: discrete signal composed from a series uncorrelated random variables with zero average, finite variance and flat power spectral density (PSD).

Solving the equation 1.1 in frequency domain gives

$$(-m\omega^2 + i\gamma_0\omega + k_0)z(\omega) = R(\omega) \tag{1.3}$$

where ω is the resonant angular frequency of the oscillator, $z(\omega)$ is the PSD of the fluctuations and $R(\omega)$ is the PSD of the thermal force.

The thermal excitation force has a constant driving strength for the entire frequency range, thus the influence of the thermal noise depends on the system transfer function [87–90] $G(w)$, that is defined as

$$G(\omega) = \frac{R(\omega)}{z(\omega)} \tag{1.4}$$

describing the relation of the response of the system to the driving force. From equations 1.3 and 1.4 the transfer function becomes

$$G(\omega) = k_0 \left(1 - \frac{\omega^2}{\omega_0^2} + i\frac{\omega}{\omega_0 Q_0}\right) \tag{1.5}$$

where $\omega_0 = \sqrt{k_0/m}$ is the eigenfrequency and $Q_0 = m\omega_0/\gamma_0$ is the quality factor of the cantilever.

From equation 1.2 the connection between the force $R(t)$ and the damping coefficient γ_0 occurs. This is known as Einstein relation [91]. It states that the drag and fluctuating forces have the same origin and cannot be treated independently. Note that the nature of damping is not considered in the analysis since it does not essentially modify the response of the flexural modes [92].

The thermal noise of the free cantilever can be calculated through the fluctuation–dissipation theorem [9, 82, 83, 87, 93–97] that relates the thermal fluctuation power spectral density S_z to the transfer function G and the temperature of the system T

$$S_z(\omega) = -\frac{2k_B T}{\omega}\Im\left(\frac{1}{G(\omega)}\right) \tag{1.6}$$

where $\Im$ denotes the imaginary part of the susceptibility $1/G(\omega)$.

The positional PSD of the cantilever from equations 1.5 and 1.6 becomes

$$S_z(\omega) = \frac{2k_B T}{k_0\omega_0}\frac{1/Q_0}{(1-\frac{\omega^2}{\omega_0^2})^2 + (\frac{\omega}{\omega_0 Q})^2} \tag{1.7}$$

From equation 1.7 stems that the noise spectrum has the form of a Lorentzian.

The mean square displacement of the cantilever due to the thermal motion $< z^2 >$ can be determined by integrating PSD $S_z(\omega)$ from equation 1.7. Using the Parseval relation [83,97,98] yields

$$< z^2 >= \int_{-\infty}^{\infty} S_z(\omega) dz = \frac{k_B T}{k_0} \tag{1.8}$$

The same relation can be obtained by using the equipartition theorem that connects the temperature of the system and the average potential and kinetic energies [87,99,100]. The equipartition theorem states that when the system is in thermal equilibrium, each degree of freedom contributes an average energy $k_B T/2$ [35,88,101]. Each eigenmode of the cantilever is a mechanical degree of freedom. Thus the potential energy of the cantilever [88] is expressed as

$$\frac{1}{2} k_0 < z^2 >= \frac{1}{2} k_B T$$

$$< z^2 >= \frac{k_B T}{k_0}$$

The mean square displacement of the cantilever given by equation 1.8 is the actual physical displacement $< z^2 >$, while the measured or virtual physical displacement $< z^{*2} >$ is different since the measurements are performed with the optical beam detection technique so the slope of the cantilever rather than the actual displacement is measured [4,86,92]. Thus the value of the measured physical displacement needs to be corrected. For the free rectangular cantilever the virtual mean deflection is defined as $< z^{*2} >= 4/3 < z^2 >$ and in the case of the pinned cantilever the virtual mean displacement becomes $< z^{*2} >= 1/3 < z^2 >$ [4]. The real situation lies between these two cases and according to the ratio between the sample and cantilever stiffnesses, the free or the pinned case is more probable [4,102].

Worth to notice that the cantilever in AFM is not a simple harmonic oscillator but has a number of eigenmodes with different eigenfrequencies ω_i, quality factors Q_i, modal stiffnesses k_i, optical detection sensitivities σ_i and damping coefficients γ_i, where i is the mode number. However, since the thermal fluctuations in different modes are uncorrelated [4,92], the preceding calculations can be applied to the higher eigenmodes [4, 88], thus allowing independent determination of the modal parameters

[103]. It is particularly useful for the modal stiffness calculations since it is a precondition for the quantitative interpretation of the spectroscopy results [88, 104–106].

The most common application of the thermally excited AFM is the non-destructive fast calibration of the spring constant of the cantilever [4,7,86,103,107–111]. However, using the thermal excitation is possible to obtain information about the conservative and dissipative tip–sample interaction or interaction potentials [6,112–114]. It has been already demonstrated that by using this method it is possible to investigate the viscosity and the density of the environments, electrostatic double-layer forces [115], viscoelastic properties of compliant samples [5, 116–119] and the local elasticity of hard surfaces [7].

1.3 Conclusions

AFM evolved from a topographical technique into a more refined tool allowing to explore the tip-sample interaction forces by studying the cantilever dynamics. Such evolution was stimulated by different reasons: the necessity to achieve lower operation forces and to improve the spatial resolution when soft samples are investigated and the need to perform rapid quantitative measurements of the surface properties.

Recently the dynamic AFM family has been enlarged by incorporating the multifrequency excitation and detection modes, where the response is composed of a sum of responses from every excited frequency and hence new characterization channels are available.

CHAPTER 2

Data analysis in Atomic Force Microscopy by Fourier and wavelet transforms

2.1 Introduction

In the present work force spectroscopy measurements in the thermally driven regime (i.e.without external excitation of the cantilever) are performed. In such experiments the jump-to-contact transition (mechanical impact composed of one or few oscillations of the cantilever tip) has been used as an example of the impulsive tip-sample interaction to prove the validity of the few cycles regime. The jump-to-contact transition occurs when the surface force gradients exceed the elastic constant of the cantilever [120]. The required acquisition time for the measurements is just few milliseconds.

The impulsive tip-sample interactions are investigated from one-shot measurement and averaging is not used. This is especially important in experiments where the sample could be permanently modified or damaged by the tip interaction. The instantaneous processes occurring while the cantilever interacts with the sample carry a wealth of information about the dynamic of the cantilever.

To retrieve information from such short single-event interaction a method of analysis which is able to follow the instantaneous changing of the rapid varying signal parameters, analyze the spectroscopy curve through the JTC transition without the interruption and perform the simultaneous analysis of all the cantilever frequencies within the bandwidth of the detection system is required.

2.2 Fourier transform

The aim of the data analysis is to explore the main characteristics of the signal by a signal transformation. A way of analyzing the detected cantilever signals in AFM experiments is to use the Fourier transform (FT), defined as [121]:

$$F(\omega) = \int_{-\infty}^{+\infty} f(t) e^{-j\omega t} dt$$

where $f(t)$ is the temporal signal, ω is the angular frequency and $F(\omega)$ is the Fourier coefficients. FT projects the recorded signal of the cantilever $f(t)$ onto a base of complex exponentials at all frequencies. In this representation the eigenmodes of the cantilever appear as resonance peaks in the FT spectrum. FT may be considered as a mathematical technique to transform the way of seeing the signal from the time to the frequency domain with the highest possible spectral resolution.

For stationary systems, where the signal properties over time do not change, the FT spectrum is easily interpreted. However, in cases where the systems change their physical properties and hence their characteristic spectrum in time, FT shows only the spectrum integrated over the acquisition time. As a consequence the modifications of the temporal signal are not directly correlated with the frequency features of the spectrum and impossible to point out the origin of a particular spectral feature in time.

Traces collected in AFM measurements usually contain non-stationary characteristics such as drifts, trends, rapid changes. For AFM these characteristics are significant parts of the signal but FT is often not able to fully display them.

For such non-stationary signals the method that combines the time and frequency domain analysis and hence shows the signal evolution in both time and frequency is needed. The windowed FT belongs to the family of techniques with such temporal and spectral resolution and it has been one of the first methods devised to operate in the time-frequency plane. However, windowed FT has the drawback of the fixed time-frequency resolution [121]. After the choice of a window function, the size of the time-frequency window is fixed, implying that the time and frequency resolution are the same at all times and frequencies.

2.3 Wavelet transform

2.3.1 Continuous wavelet transform

The wavelet transform (WT) is a mathematical approach that gives the time–frequency representation of a signal [121–123]. WT is an improved alternative to the windowed FT. This analysis provides the representation of the energy associated to the signal at specific time and frequency (i.e. shows the correlation between the spectral features and the temporal evolution of the signal) and gives the possibility to adjust the time-frequency resolution. WT may be considered as the time-frequency analysis method with an adjustable window.

Wavelet is a waveform function $\Psi(t)$ with limited support in time and zero average [121]

$$\int_{-\infty}^{+\infty} \Psi(t)dt = 0$$

The zero average indicates that $\Psi(t)$ is an oscillating function. Sinusoids, which are the basis of FT, in opposition to the basis of wavelets, are not limited: they continuously spread from minus to plus infinity. Sinusoids are periodic and smooth; wavelets are not periodic and may have discontinuous derivatives. Obviously, the signals with rapid changes are analyzed better with the non-periodic wavelets.

The WT is defined as the projection of the time signal $f(t)$ onto a set of functions $\Psi_{s,d}(t)$ obtained from the translations and dilations of the original wavelet $\Psi(t)$. The function $\Psi(t)$ is called a mother wavelet, functions $\Psi_{s,d}(t)$ are called daughter wavelets and are determined as

$$\Psi_{s,d}(t) = \frac{1}{\sqrt{s}}\Psi\left(\frac{t-d}{s}\right)$$

where s is the positive adimensional scale parameter and d is the delay [121]. The scale parameter stretches or compresses the mother wavelet and is connected to the frequency (low scale gives compressed wavelet and thus it can better analyze rapidly changing features what means high frequency components of a signal and vice versa). The delay parameter shifts the wavelet along the time axis and is connected to the time. Both parameters vary continuously.

The projection of the signal over scaled and delayed version of the

mother wavelet is the WT of the signal [121]

$$W^f(s,d) = \int_{-\infty}^{+\infty} f(t)\Psi^*_{s,d}(t)dt = \int_{-\infty}^{+\infty} f(t)\frac{1}{\sqrt{s}}\Psi^*\left(\frac{t-d}{s}\right)dt$$

wavelet coefficients $W^f(s,d)$ are functions of scale and delay, and since these parameters vary continuously, this transform is called continuous wavelet transform (CWT). Wavelet coefficients $W^f(s,d)$ measure a relative similarity between the signal and the wavelet function at specific delay and scale and the higher coefficient denotes the higher similarity.

The square modulus of the wavelet coefficients $|W^f(s,d)|^2$ is called scalogram and depicts the local energy density of the signal at the given scale and delay. CWT converts one dimensional temporal signal into two dimensional time-frequency representation [121].

CWT is a windowing technique allowing to use the stretched wavelets where necessary to capture information from the low frequency components of the signal, and the compressed wavelets for the high frequency parts. Worth to notice, the basis of CWT is not unique and should be chosen according to the characteristics of the signal.

Since CWT operates in two-dimensional space, both time and frequency resolutions have to be considered and such resolutions depend on the wavelet choice. Time and frequency resolutions cannot be improved simultaneously: when the frequency resolution increases, the time resolution decreases, as a consequence of the time-frequency uncertainty principle [124].

In this work Gabor mother wavelet is used because it has the best time–frequency resolution [125, 126]. Gabor wavelet is a complex frequency-modulated Gaussian function [121, 126]

$$\Psi(t) = \frac{1}{\sqrt[4]{\pi\sigma^2}} exp\left(-\frac{t^2}{2\sigma^2} + i\eta t\right)$$

where σ and η are parameters which control the time spread and carrier frequency of the wavelet and multiplied together constitute a dimensionless parameter called the Gabor shaping factor

$$G_s = \sigma\eta$$

The G_s parameter determines the envelope of the mother wavelet and the time–frequency resolution. Gabor wavelet with the shaping factor

$G_s = 5$ (known as the Morlet wavelet) [121] is used in the following analysis. Such choice of parameters provides the balance in the time-frequency resolution and is generally suitable for various types of signals [126].

To exemplify the advantages of wavelet transform in comparison with Fourier transform, the analysis of chirp signals [127] with frequencies changing linearly from 2 kHz to 10 kHz in time intervals of 10 ms is shown (figure 2.1).

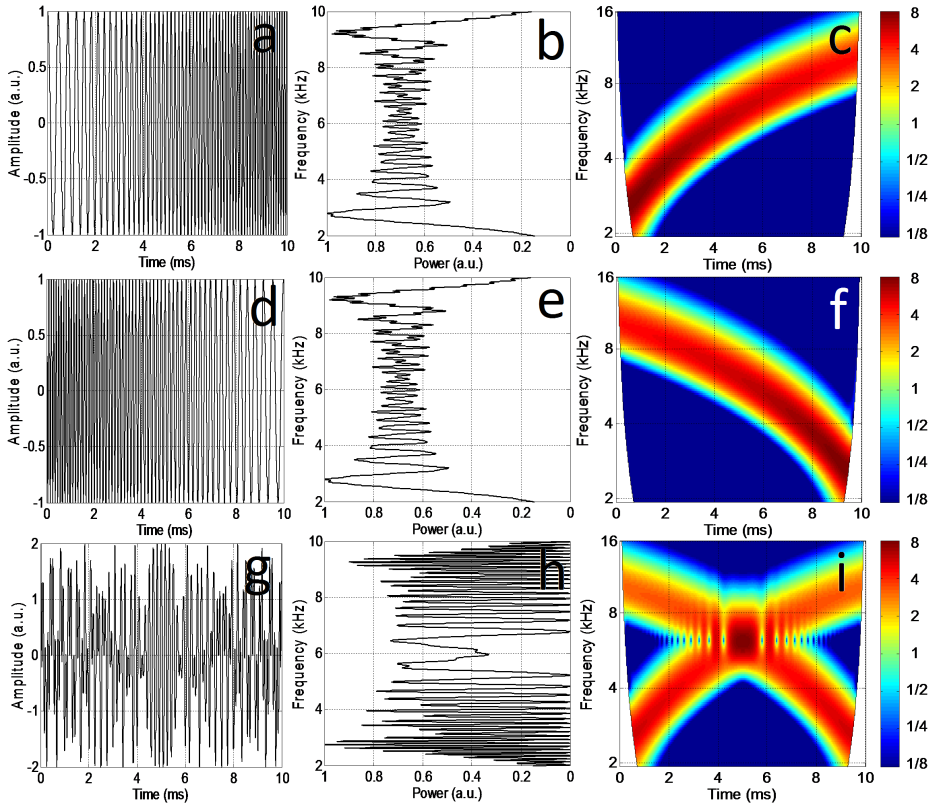

Figure 2.1: (a) Up-chirp signal swept from 2 to 10 kHz. (d) Down-chirp signal swept from 10 to 2 kHz. (g) Sum of the chirps signal shown in (a) and (d). (b,e,h) Fourier transforms of the signals shown in (a,d,g), respectively. (c,f,i) Wavelet transforms of the signals shown in (a,d,g), respectively. Wavelet coefficients are coded in a color-scale. Both colors and frequencies are represented in octaves, i.e. base 2 logarithmic scales.

Figures 2.1a,d represent the up-chirp and down-chirp signals in time domain. Figures 2.1b,e are FTs of the signals and as can be seen they are

identical. This is due to the fact that the spectral components of the signals are equal, so by looking on FT power spectra it is impossible to distinguish up-chirp and down-chirp signals. Instead, the WT magnitudes of the same signals (figures 2.1c,f) are different and it is easy to relate them to the signals.

When only one chirp signal in the time domain is present, it is possible to tell which one is the up-chirp and which one is the down-chirp signal (figures 2.1a,d). The signal from the figure 2.1g is a sum of the signals in figures 2.1a,d. From the time domain representation it is difficult to conclude about the dynamics of the signal as well as by looking at the FT power spectrum (figure 2.1h). Instead, the WT of the signal in figure 2.1i shows the presence of two chirps that compose the signal.

This illustrates the advantages of WT in comparison with FT analysis when short and rapidly varying signals need to be investigated.

2.3.2 Cross-correlation wavelet transform

To get the full spectral response of the signal the phase analysis need to be performed simultaneously with the amplitude analysis. The phase analysis of a non-periodic motion is based on the cross-wavelet transform (XWT) and the concept of "phase carpet".

The cross-wavelet spectrum of two time signals $h(t)$ and $g(t)$ is defined as

$$W^{hg}(s,d) = W^{h}(s,d)W^{g*}(s,d)$$

where $W^h(s,d)$ and $W^g(s,d)$ are the wavelet transforms of the signals and $*$ denotes the complex conjugate. The wavelet coefficients are complex numbers that can be represented as

$$W^{h}(s,d) = |W^{h}(s,d)| \exp(\Phi^{h}(s,d))$$

where $|W^h(s,d)|$ is the wavelet amplitude and $\Phi^h(s,d)$ is the absolute phase. Both power and phase pertain to the "point" (s,d) in the frequency-time plane. Regions in the time-frequency space where the time series concentrate power in the same spectral range and at the same time have high cross-wavelet amplitudes, $|W^{hg}(s,d)|$, for short, they have a high common energy.

The relative phase difference between the two time series at specified time-frequency point (s,d) can be calculated as

$$\Phi^{hg}(s,d) = \Phi^{h}(s,d) - \Phi^{g}(s,d) = \tan^{-1}\left(\frac{\Im(< s^{-1}W^{hg}(s,d) >)}{\Re(< s^{-1}W^{hg}(s,d) >)}\right)$$

where $\Phi^{h}(s,d)$ is the phase of h, $\Phi^{g}(s,d)$ is the phase of g, $<>$ represents the smoothing operator, $\Re$ and $\Im$ are the real and imaginary parts, respectively. This definition, as in optical coherence [128], depends on the smoothing operator. A discussion on this technical aspect can be found in [129, 130].

Impulsive signal is composed of a superposition of a number of Fourier components oscillating at different frequencies. The phases associated with these oscillating components could be measured if a reference signal at the same frequency is available for each one of them, i.e. if the impulsive signal could be compared with the reference constituted by monochromatic components with a known phase (the "phase carpet" reference).

The sinc ("sinus cardinalis") function, expressed as $A\sin((t-t_0)/a)/((t-t_0)/a)$, where a is the shape parameter that controls the width of the function centered at time t_0 and A is the peak amplitude, constitutes good phase reference function. Taking as a measure of the time width Δt the distance between the first zero-crossings at either side of the maximum $\Delta t = 2\pi a$ is obtained.

The sinc function can be expressed as a sum of cosines that have a maximum in $t = t_0$ and oscillation frequencies in the interval between zero and maximal cut-off frequency $f_m = 1/a$. According to the indetermination principle, the wider the frequency span, the narrower the time extension of the sinc function. Each one of the cosines that build up the sinc function is used as the phase reference. In particular, the sinc function represents the phase reference around the time t_0, where the amplitude of the signal is different from zero. To show an example of this analysis, a signal composed by the sum of three cosines oscillating at different frequencies, $f_1 = 1/T$, $f_2 = 2f_1$, $f_3 = 4f_1$ (T is the oscillation period), with unit amplitude and zero phase at time zero is considered.

Figure 2.2a shows the signal plus the sinc function centered at time zero. In figure 2.2b the wavelet cross-correlation analysis is shown. The three peaks in the cross-correlation spectra correspond to locations in the

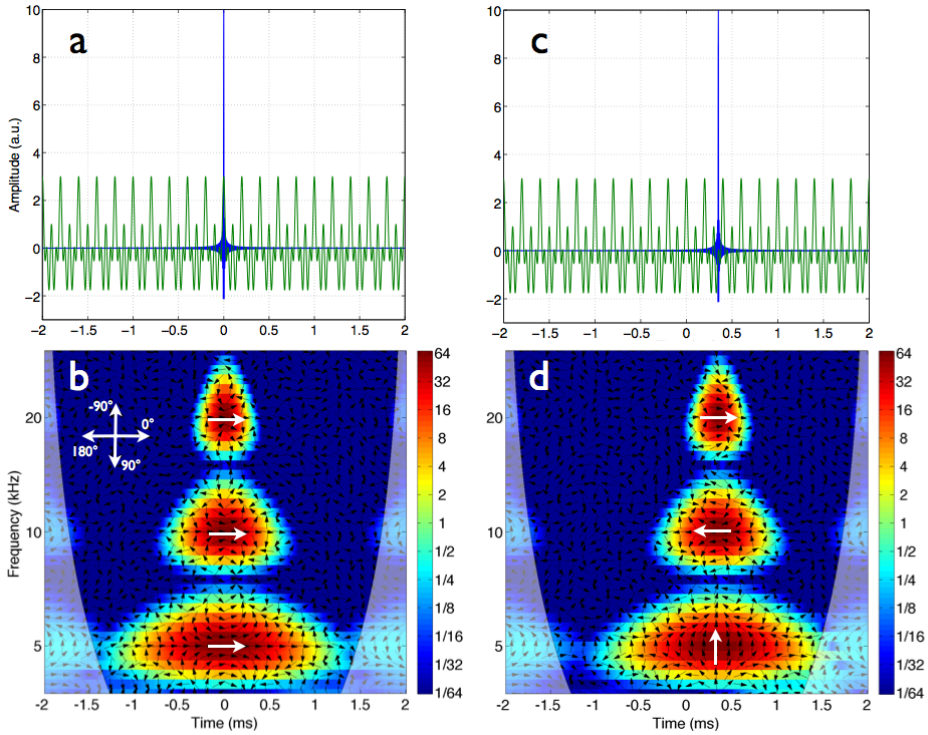

Figure 2.2: (Adapted from [33]) The signal (continuous green line, panels a and c) is composed by the superposition of three cosines with zero initial phase and frequencies $f_1 = 1/T$, $f_2 = 2f_1$, $f_3 = 4f_1$, where T is the oscillation period and $f_1 = 5$ kHz. The sinc function is centered at time zero (panel a) and at $7/4T = 350\mu$s (panel c), with amplitude A=10 and shape parameter a=3.33 μs. In panels b and d the wavelet cross-correlations between the signal and the sinc are shown. The amplitude in the cross-correlations is coded in color scale and represents a measure of the energy concentration in the same spectral range and at the same time by the correlated functions. The relative phase is represented by the slope of the arrows (see legend in panel b). The white arrows highlight the phase-shift at the maximum cross-correlation amplitude at the cosines frequencies. The areas where edge artifacts may distort the wavelet representation are delimited by a lighter shade.

time-frequency plane where both the signal and the reference function have high common spectral energy. The peaks frequencies are those of the cosines forming the signal, their temporal alignments correspond to the location of the sinc function. Their temporal and frequency width are limited by the time resolution of the analyzing wavelets [125, 131]. The

slope of the arrows superposed on the cross-correlation spectra measures the local phase difference between the signal and the reference sinc. In this case the sinc is centered around zero and each Fourier components in the signal is in phase with the cosines forming the sinc function, as is verified by looking at the local phase in the points of maximum correlation energy (arrows pointing right). Moving the sinc center alters the phase relations between the Fourier components forming the signal and those forming the reference function. Figure 2.2c shows the signal and the sinc function centered at time $7/4T$ and in figure 2.2d the wavelet cross-correlation analysis is shown. While the intensity of the three correlation peaks has not been altered, the phase relations have been modified. Moving the reference function by $7/4T$ allows to verify that the phase difference at f_3 is unchanged, at f_2 is π and at f_1 is $-\pi/2$.

The wavelet transforms may show inaccurate representation of signal near the edges that delimits its temporal duration, because of the convolution of the wavelet with a sharp discontinuity in the signal. The areas in the time-frequency plane where edge artifacts may distort the wavelet coefficients are delimited by a lighter shade, as in figures 2.2b,d. Note that in all the wavelet graphics, the frequency axis and the amplitude color scale are base-2 logarithm scales, representing the axis or color scale values in octaves.

2.4 Conclusions

It is important to examine the possibility to study the single-event rapid interactions to stimulate the future developments of the AFM.

The present work is dedicated to the introduction of the wavelet transform as the new tool for the data analysis in dynamic force spectroscopy. This intuitive and effective method of signal analysis can be used in different multifrequency AFM experiments to push further the processes of understanding of the cantilever dynamics and thus to lead toward the design of the next generation of AFM techniques.

Part II

Experimental results

CHAPTER 3

Experiment

3.1 Experimental set-up, samples and conditions

The experiments consist in acquiring the deflection signal of the thermally driven cantilever while the sample is moved towards the tip at a constant velocity. During the measurements the tip-sample interaction forces modify the Brownian motion of the cantilever. The modifications in the thermal noise spectrum contain information about the interaction forces and are used to investigate the tip-sample interactions [5, 7]. The scope is to acquire the signal across the JTC transition and the subsequent impact, that occurs when the surface force gradients exceed the cantilever stiffness [2].

The experiments are performed on three different surfaces: a) freshly cleaved Highly Oriented Pyrolytic Graphite (HOPG) surface, b) Silicon (Si) surface, c) PolyEthylene Terephthalate (PET) surface. Experiments are performed in air under ambient conditions (55% relative humidity, 296 K room temperature and atmospheric pressure), with the rectangular Au-coated silicon cantilever (the plan view dimensions 458 x 42 μm^2 have been measured by using an optical microscope). For the rectangular cantilever the modulus of elasticity can be calculated through the spring constant and the geometrical parameters of the beam: $E = (4kL^3)/(ab^3)$. For the silicon cantilever used in the experiments the Young's modulus is $E = 160\ GPa$. This value is in the range of the typical elasticity of the silicon. The cantilever spring constant $k = 0.14 \pm 0.02\ N/m$ is measured using both Sader [132] and thermal tune [4, 86] methods applied to the first flexural eigenmode. The inclination of about 15° of the cantilever with respect to the sample surface has been taken into account [133] in cal-

ibrating the spring constant. The rms amplitude of thermal oscillations is about 2 Å at room temperature.

The microscope system is equipped with an isolation box, providing thermal and acoustic isolation. The system stands on a spring-suspended platform for shielding from the external mechanical noise. The cantilever deflections are measured by a standard optical beam deflection system. Light from the laser diode ($\lambda = 600\ nm$) reflects from the cantilever and is monitored by the four-section quadrant photodiode [26]. Differential voltage outputs from the photodiode are collected with the up–down sectors. The total bandwidth of the beam detection system exceeds 1 MHz. The scanning system is based on a single piezotube with the maximal vertical extension range of $2\ \mu m$.

The cantilever deflection signal from the photodiode is sampled with a digitizing oscilloscope and in this experiment traces are recorded at the sampling frequency of 10 MS/s.

3.2 Force spectroscopy measurements

The atomic force microscopy is a powerful tool which allows not only to image the topography of surfaces at high resolution nearly for all types of samples, but can also provide maps of the local physical, chemical and mechanical surface properties with quantitative results by measuring different kinds of forces (like van der Waals and Casimir forces, adhesion, elasticity, capillary, magnetic) [120, 134]. Using AFM in such force measurements is commonly known as force spectroscopy, and these curves are called force curves. This technique has brought a major effect in many areas of science and now AFM is presented as an essential tool for nanotechnology.

To obtain the force curve, a direct measurement of the tip-sample interaction forces as a function of the distance between the tip and the sample is performed. To do so, the tip is approached to the sample surface and the consequent deflection of the cantilever is recorded as a function of the piezoelectric displacement. This curve shows the cantilever Brownian motion superimposed on the static deflection of the cantilever. From the cantilever deflection the force can be measured using Hooke's law [135].

To convert the output voltage signal from the quadrant photodiode of the beam deflection method to the cantilever deflection in nm, the inverse

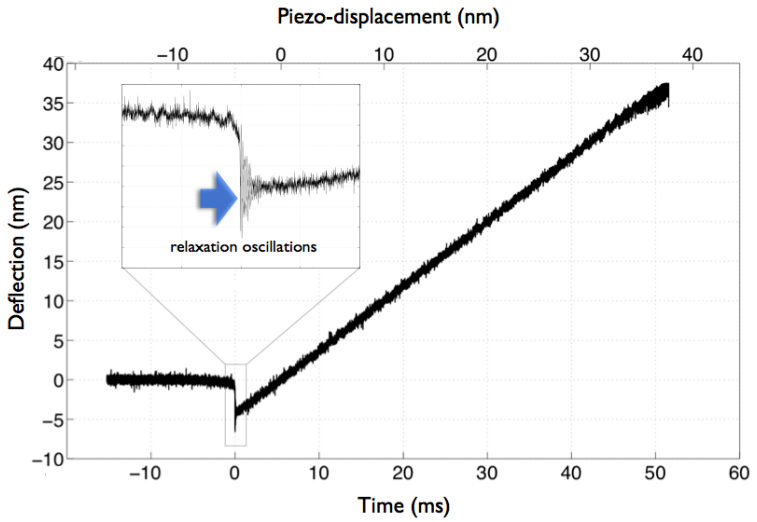

Figure 3.1: (Adapted from [33]) Deflection of the cantilever as a function of time during the force curve (constant approach velocity $0.817nm/ms$). Time zero is centered on the jump-to-contact transition, positive times span the contact line. In the inset a zoom on the relaxation oscillations after the jump-to-contact transition. The vertical scale is calibrated only for the first flexural mode and does not apply to the relaxation oscillations.

optical lever sensitivity (InvOLS) (calibration constant with dimension of nm/V) is needed [47].

The InvOLS has been measured as the inverse slope of the linear contact part of the standard force measurement made on a hard substrate, when the tip pushes on the surface. In this case the distance moved by the piezo-scanner is equal to the cantilever deflection, neglecting indentation. It is important to note that the shape of the first flexural mode very nearly matches the shape of the bent cantilever when the tip is in contact with the surface. For this reason the measured InvOLS (250 nm/V) can be used to calibrate the bending of the first flexural mode only.

A typical force curve [134] obtained during a loading cycle is shown in figure 3.1. It is possible to observe the Brownian oscillations of the cantilever around the instantaneous equilibrium position while it approaches the surface at constant velocity. Note two distinctive features, the horizontal line of zero deflection, representing the free not deflected cantilever, and the sloped linear contact line. Between them, at a distance of few nanometers from the surface, the cantilever is subject to a JTC tran-

sition, an instability caused by the surface forces. The jump-to-contact transition takes place when the gradient of the surface forces exceeds the elastic constant of the cantilever. The jump is identified by a sharp downward deflection following the horizontal line of zero deflection. After the jump-to-contact the tip is in contact with the surface, the cantilever is statically bent and follows the piezo displacement. The bottom abscissa in figure 3.1 shows the time zeroed at the jump-to-contact point so that negative times refer to the cantilever before the jump-to-contact, positive times refer to the cantilever after the jump-to-contact. The top abscissa shows the piezo displacement zeroed at the point of zero-deflection after the jump-to-contact.

The motion after the JTC transition consists of a sharp acceleration towards the surface and a concomitant impact of the tip with the surface. It is precisely this single event that is studied in this work, to demonstrate that enough information can be captured to reconstruct the tip trajectory on impact. In the inset a magnification of the tip-sample impact, with the characteristic relaxation oscillations, is shown (figure 3.1). Since the measured InvOLS is used to calibrate the deflection of the first flexural mode but not the deflection of the higher modes, that have different shapes, the ordinates in the graph do not relate to the relaxation oscillation that, as will be shown, are caused by the excitation of the higher modes.

CHAPTER 4

Complex eigenmodes dynamics of the interacting cantilever resolved by wavelet transform

4.1 Introduction

Traditionally the analysis of temporal traces is performed with the Fourier transform (see section 2.2), which breaks down temporal fluctuations of the cantilever into constituent sinusoids of different frequencies, i.e. the eigenmodes of the cantilever are displayed in the spectrum as resonance peaks. However, the spectral analysis provided by the FT gives a correct interpretation only in the case of stationary systems (the signal properties do not change over time). In transforming to the frequency domain by FT, time information is hidden (it is difficult or impossible to correlate particular spectral feature to its origination in time) and the Fourier spectrum displays an average of spectra corresponding to the evolution of the system during the acquisition time interval. AFM force curves contain numerous non-stationary or transitory characteristics such as the jump-to contact transition during the approach curve. These characteristics are important part of the signal, and Fourier analysis is not suited to show them.

A powerful and well developed mathematical tool that combines time and frequency domains is the wavelet analysis (see section 2.3). Previously, wavelet analysis has been used in atomic force microscopy mainly to denoise or extract data from images, which is up to now the most important application of the wavelet transform. However, using the WT in force spectroscopy allows to represent the temporal evolution of the spectral content of the oscillating cantilever and measure its frequency shift due to the interaction with surface force gradients. It is very useful

because the correlation of the spectral features with their temporal dynamics could provide a new significant knowledge about the cantilever behavior across the jump-to-contact transition. Moreover, simultaneous analysis at all frequencies reduces the acquisition time.

In this chapter, the wavelet transform method is introduced as an advanced tool for the analysis and characterization of temporal traces obtained during force spectroscopy in the thermal driving regime. The transient eigenmodes analysis is performed by using the combined Fourier and continuous wavelet transform (see section 2.3.1) approaches with an acquisition times as short as few milliseconds.

4.2 Transient eigenmodes analysis combining Fourier and wavelet transforms

The cantilever deflection versus time (figure 4.1a) is captured during the tip approach to the sample surface at constant velocity. Analyzing the wavelet spectra immediately after the jump-to-contact transition, the dynamics of the cantilever flexural modes due to the impact is observed. Interestingly the observed dynamics depends on the surface wettability and ambient conditions.

Before focusing on the analysis of the cantilever dynamics on various surfaces, an in-depth description of the cantilever dynamics on the HOPG surface is described, as representative of the general trend following the JTC transition.

The analyzed signal (figure 4.1b) is a zoomed region around the tip–sample impact. The signal is caused by the Brownian motion of the cantilever around the instantaneous equilibrium position, the static deflection of the cantilever due to a combination of forces acting on the tip near the sample surface and the relaxation oscillations after JTC. The zero of the time scale coincides with the JTC transition, identified by a sharp downward deflection of the signal curve. Negative times correspond to the free cantilever approaching the surface, positive times to the cantilever in contact with the surface after the JTC transition. Accordingly, three regions of the signal curve can be distinguished, all under thermal excitation: a) free cantilever motion, b) instability region where long-range forces affect the cantilever dynamics and lead to the JTC transition, c) ensuing contact curve, where the tip is in contact with the surface

and the bent cantilever is under the action of short-range adhesion forces. From the signal vs time in figure 4.1b is inferred that the sharp downward deflection (of about 5 nm) associated to the JTC transition takes around 10 μs and it may be considered as an instantaneous process on the typical time scales of the cantilever oscillation period. The maximum static load force is $F_{load} = -0.75\ nN$ and it is negative since an adhesion force is responsible for the JTC transition, which is opposite to the elastic force of the cantilever (figure 4.1a).

During the tip interaction with the surface and the successive impact, the cantilever eigenmodes structure is continuously changing due to the modification of external forces and boundary conditions. As an example, consider the frequency downshift of the first eigenmode due to the attractive forces just before JTC and the abrupt change in the boundary conditions just after JTC, from the free cantilever to the cantilever with the tip pinned at the surface (see figure 4.1) [4, 102]. To refer unambiguously to the cantilever eigenmodes, need to differentiate between "long-lived eigenmodes" and "excited eigenmodes". Long-lived eigenmodes are modes belonging to the free cantilever (before JTC) or to the pinned cantilever (after JTC). Excited eigenmodes are transient modal structures, due to the action of the surface forces and the impact forces, occurring in the time span of the JTC transition.

In figure 4.1c are shown the FT spectra of the signal represented in figure 4.1b. Note that since FT is a time invariant operator and is described as a highly non-stationary process, the FT spectra are an average over a $5\ ms$ time interval and do not convey information on the spectral evolution in time. Instead, the wavelet time–frequency analysis in figure 4.1d follows the evolution of the spectral content of the cantilever deflection signal and measures the frequency shift caused by the acting forces and force gradients on the tip during the measurement. It is interesting to note that in the time interval under consideration, after the JTC transition, the piezo actuator moves the sample at constant velocity by approximately $5\ nm$, reducing the static (negative) load from maximum to zero. As seen in figure 4.1d, the variation of the static load has no effect on the modal structure of the thermally excited cantilever.

On the WT spectrum in figure 4.1d are visible at negative times the thermal oscillations of the first (12.01 kHz) and the second (79.67 kHz) flexural modes (black-dashed lines). The JTC process is accompanied by

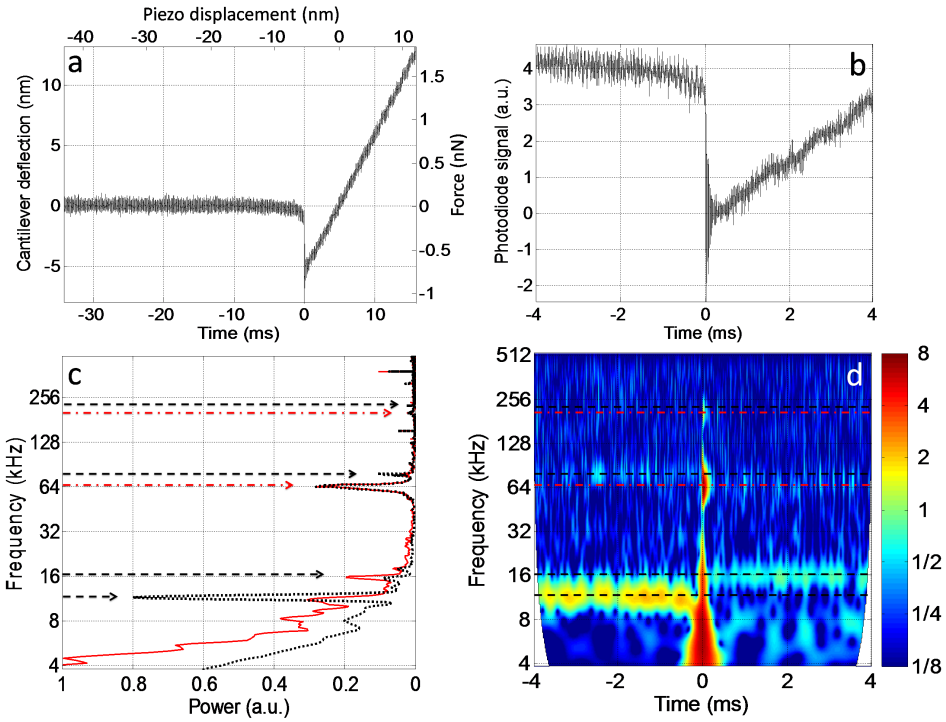

Figure 4.1: (a) Deflection (force) of the cantilever as a function of time (sample displacement). (b) Relaxation oscillation of the cantilever. Deflection is given in arbitrary units (a.u.) because only the deflection of the first flexural mode is calibrated and not that of higher modes which contribute to the relaxation oscillations. (c) Fourier transforms of the cantilever deflections reported in (b). Black dotted line: before JTC including the impact zone, time interval from $-4\ ms$ to $1\ ms$. Continuous red line: after JTC including the impact zone, time interval from $-1\ ms$ to $4\ ms$. (d) Wavelet transform of the cantilever deflections reported in (b). Wavelet coefficients are coded in a color-scale. Both color-scale and frequencies are represented in octaves, i.e. base 2 logarithmic scales. Time zero corresponds to the jump-to-contact transition in all frames. Black dashed lines correspond to flexural long-lived eigenmodes of the free and interacting cantilever (numerical values are reported in table 4.1). Red dash-dotted lines are associated with spectral features of the cantilever excited eigenmodes due to the JTC impact.

the spectral broadening of the first mode in the region from 1 to 34 kHz. The impact excites for a short time the second (67.92 kHz) and the third (203.48 kHz) modes of the cantilever (red dash-dotted lines). Moreover, after the JTC transition, the resonance at frequency a little higher than

the first flexural mode (16.98 kHz) and the higher resonance at nearly the same frequency as the second free cantilever mode are identified (black-dashed lines).

The presence of these resonances is interesting because they cannot be explained as modes of the pinned cantilever and hint to a complex interplay between the tip and the surface kept in ambient conditions that influence the contact dynamics of the cantilever. It is discussed in details in the next section.

To assign the peaks in the Fourier spectra near the JTC transition (figure 4.1c), is taken advantage of the WT. In particular, some of the highest peaks in the FT spectrum do not correspond to long-lived eigenmodes because very short non-stationary signal is analyzed and in this time interval much of the signal energy consists in "bumps" next to JTC due to the excited cantilever modes. Since the FT is not providing the representation of the temporal evolution of the frequency modifications, it is not easy to correctly assign the Fourier peaks to excited eigenmodes or to long-lived eigenmodes on the basis of the FT only. Instead, WT enables to attribute the origin of the peaks spotted in the FT since their temporal evolution is unraveled.

4.3 Spring-coupled cantilever dynamics resolved by wavelet transform

After the JTC transition the tip of the cantilever comes into the contact with the sample surface and surface forces responsible for the tip-sample interactions come into play. In this case, the cantilever tip can be described as pinned or spring-coupled to the surface [102,136] and appropriate boundary conditions must be chosen. The spring-coupled state of the cantilever occurs if, due to the conditions of the contact, the cantilever is forced to oscillate either because of the sample surface vibrations or because the adhesion forces are not able to fully adhere the tip to the surface. The oscillation amplitudes are small (of the order of 0.1 nm) and the tip-sample interaction force can be rationalized as a linear spring with elastic constant k^*, where k^* is the negative of the derivative of the tip-sample force relative to the static equilibrium position of the cantilever [27]. From this point of view, the free cantilever state corresponds to $k^* = 0$ (infinitely soft spring) and the pinned cantilever to $k^* = \infty$ (infinitely stiff spring).

Table 4.1: Frequencies and frequency ratios of the flexural modes measured from FT spectra for the free cantilever f_i and the spring-coupled (interacting) cantilever $f_i^{'}$. Frequency ratios are given in units of the first free flexural eigenmode. The theoretical frequency ratios (theo.) [4] for the free and pinned cantilever are reported for comparison.

Mode i	f_i (kHz)	f_i/f_1	$f_i^{'}$ (kHz)	$f_i^{'}/f_1$	f_i/f_1 (theo. free)	f_i/f_1 (theo. pinned)
1	12.01	1	16.98	1.41	1	4.38
2	79.67	6.63	80.77	6.72	6.27	14.21
3	212.01	17.65	214.71	17.87	17.55	29.65

Knowledge of k^* allows to calculate the tip-sample force and also get quantitative information about the elasticity of the "contact area" on the sample surface. The characteristic equation for this system (it is assumed that the forces act as a point force on the end of the cantilever) can be written as [102]:

$$\cos(k_nL)\sinh(k_nL) - \sin(k_nL)\cosh(k_nL) = (k_nL)^3k/(3k^*)(1+\cos(k_nL)\cosh(k_nL)) \quad (4.1)$$

where n is the mode number, k_n is the wave number of the flexural mode n, L is the length and k is the spring constant of the cantilever. The characteristic equation determines the value of k_nL, depending on the value of k^*. The shifted flexural resonance frequencies $f^{'}$ are calculated through the relation [102]:

$$f_n^{'} = (k_nL)^2/(2\pi L^2\sqrt{\frac{\rho ab}{EI}}) \quad (4.2)$$

where a and b are the width and the thickness of the beam, ρ is the mass density of the material of the cantilever, $I = ab^3/12$ is the area moment of inertia and E is the modulus of elasticity of the cantilever. As a result, by measuring the frequency shift after the tip-sample interactions, it is possible to retrieve the tip-sample interaction spring constant k^*. As shown in figure 4.2a the flexural eigenfrequencies of the cantilever in contact increase with respect to those of the free cantilever when $k^* > 0$ (repulsive regime), decrease when $k^* < 0$ (attractive regime). If k^* is less than or of the same order of k it has almost no influence on the higher modes and affects mostly the first flexural frequency of the cantilever [102]. This

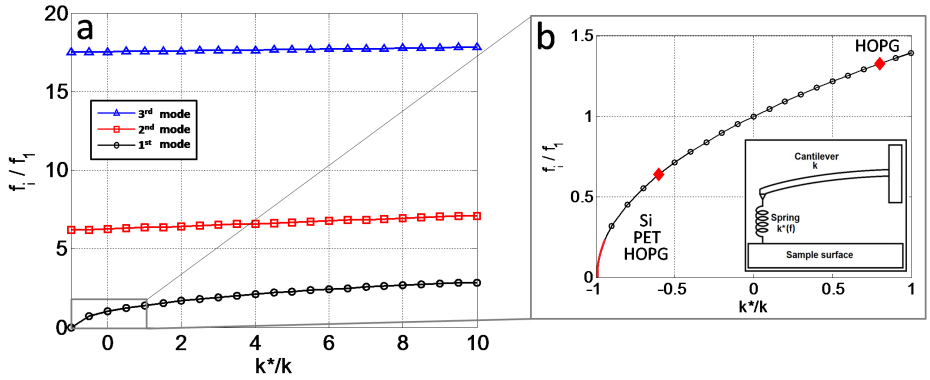

Figure 4.2: (a) Flexural eigenmodes f_i of the spring-coupled cantilever in units of the first free resonance frequency f_1 as the function of the tip-sample interaction constant k^* in units of the first free eigenmode elastic constant k. (b) A close up of the first eigenmode around the measured resonance frequencies. The red line and marks point out the observed resonance frequencies.

explains why after JTC the measured spectrum is very similar to that of the free cantilever and the typical spectrum of the pinned cantilever is not observed.

To measure the frequencies shifted by the tip-sample interaction, consider figure 4.1 where the FT and WT transforms show the signal spectra in a small regions around the JTC transition. Numerical values for the frequencies of flexural eigenmodes are reported in table 4.1.

In figure 4.2 the resonance frequencies of the spring-coupled cantilever are expressed as a function of k^*/k. In the present case the shifted first flexural mode after JTC corresponds to the ratio $k^*/k = 0.8 \pm 0.2$, where the error takes into account the experiment to experiment repeatability. Note that the value of k^* depends very sensitively on the length of the beam, that should be measured for each cantilever. Using the point-mass model [2, 102], the contact stiffness can be determined from the shift in frequency of the first flexural mode after JTC as

$$k^*/k = f_1'^2/f_1^2 - 1$$

which yields $k^*/k = 1 \pm 0.2$ (see table 4.1), in fair agreement with the beam theory.

In the present experiment the elastic constant k^* that characterizes the tip-sample interaction most probably originates from a superposition of

the electrostatic forces and capillary forces due to the condensation of atmospheric water vapor. Note that in the time span after JTC analyzed in figure 4.1d the cantilever is still under the combined actions of the adhesion forces and the elastic forces of the downward deflected cantilever, therefore the overall resulting load force is negative.

Besides the measurements of k^*, the WT allows also to estimate the tip sample force gradient k_{ts} responsible of the down shifting of the first flexural frequency before the JTC transition. Figure 4.1d shows that in the time region before JTC the instantaneous frequency of the first flexural mode is continuously shifting down, a dynamic that cannot be followed on the FT spectrum. Immediately before the JTC transition the frequency shift for the first flexural mode is $\Delta f_1 = 3.5kHz$. Each flexural mode is equivalent to a mass spring system [137].

The tip-sample interaction force gradient $k_{ts} = dF_{ts}/dz$, where F_{ts} is the tip-sample force and z is the tip-sample distance, is expressed as a function of the resonant frequency of the first flexural mode [2]

$$k_{ts} = k((f_1 - \Delta f_1)^2/f_1^2 - 1)$$

Using the observed frequency shift $k_{ts} = 0.07\ N/m$. This value is in agreement with similar measurement reported in the literature [131] and interestingly is about half the stiffness required to cause the JTC transition, suggesting that JTC is not entirely due to the surface electrostatical forces (van der Waals interactions), but requires other adhesion forces as the capillary condensation forces. At an ambient relative humidity near 50% the Kelvin diameter of the condensed water nanodrops is about 4 nm [138], which is the observed JTC distance in this experiment. This observation supports the scenario that a liquid bridge between the tip and the sample is responsible for the JTC transition.

The application of the WT technique requires a signal amplitude exceeding that of the environmental noise. This is due to the fact that in WT averaging is absent, as opposed to the FT case. The preceding analysis is an example of the single measurement with duration of few milliseconds, from which the WT is able to retrieve data that other techniques lose and to provide the wealth of information on the system.

4.4 Describing tip-samples impacts by using wavelet transform

The cantilever response after the JTC transition is influenced by the type of surface on which the tip impacts. In figure 4.3 are shown the spectral responses of the cantilever for HOPG, Si and PET. Observing the FTs of the cantilever deflection signal after JTC (figure 4.3a,c,e), note, that in all samples the impact excites two oscillations both at lower frequencies than the cantilever first free flexural mode (f_1). The first is a spectral peak observed around 8.2 kHz, very sharp and with the high contrast in PET, more broadened and with less contrast in Si and HOPG. The second is a broad peak around 1-3 kHz, with the high contrast in Si and PET and much lower contrast in HOPG. Besides that, a sharp oscillation mode at frequency higher than f_1 is present for the HOPG surface only. In all cases the higher order modes are much less affected by the surface properties and have a behavior very similar to that described for HOPG in the preceding section. In addition, the frequency downshifting of the first mode just before JTC in the various materials (figure 4.3b,d,f) can be described along the lines shown in the preceding section.

To rationalize these findings as a whole, a simple qualitative model of the interaction is proposed that takes into account the principal features deduced from the experiments and well established assumptions regarding the tip-sample interactions in air [138–140]. The key point is the observation that an attractive tip-sample interaction, leading to oscillations at frequencies lower than f_1, is associated to a negative contact stiffness. Such situation occurs when the attractive force is of the inverse n-power law type (van der Waals has $n = 2$), or in general when the elastic force modulus decreases elongating the spring. This is contrasted with the Hertz regime, when short-range hardwall-like repulsive forces results in a positive contact stiffness.

In the experiments two resonances lower than f_1 are measured, one around 1-3 kHz and the other at 8.2 kHz. To explain the presence of both resonances, the presence of a dispersive stiffness is assumed, i.e. negative linear spring with stiffness depends on excitation frequency. The mechanism of such dispersive stiffness is most probably provided by a nanosized water drop around the tip that acts as the frequency-dependent negative spring, responding with different stiffnesses according to the excitation frequency. The water condensation into drops has twofold action:

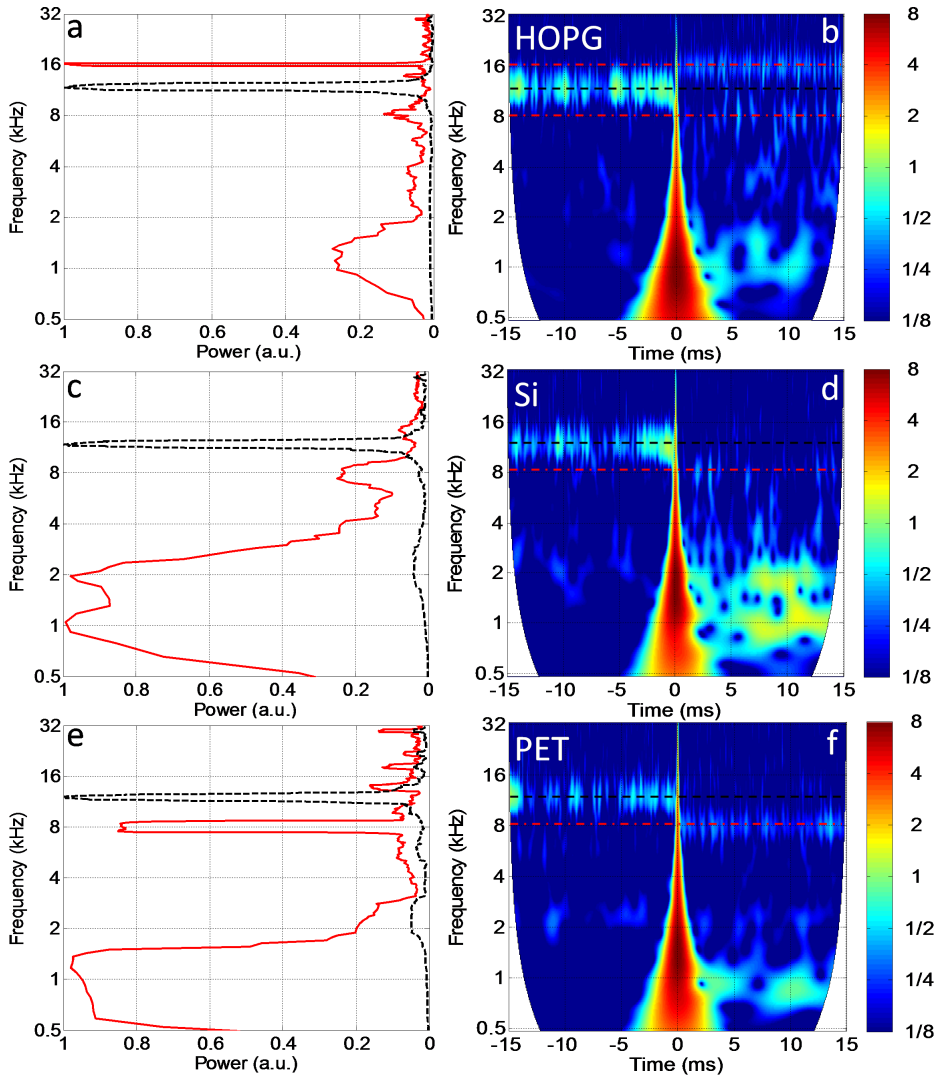

Figure 4.3: (a, c, e) Fourier transforms of the cantilever deflection for HOPG, Si and PET, respectively, before (black dashed line) and after JTC (red line). (b, d, f) Wavelet transforms of the cantilever deflection around the JTC for HOPG, Si and PET, respectively. Black dashed lines correspond to flexural eigenmodes of the free cantilever, red dash-dotted lines to the interacting cantilever (numerical values are reported in 4.1). Time zero corresponds to the JTC transition in all frames. Wavelet coefficients are coded in a color-scale. Both colors and frequencies are represented in octaves, i.e. base 2 logarithmic scales.

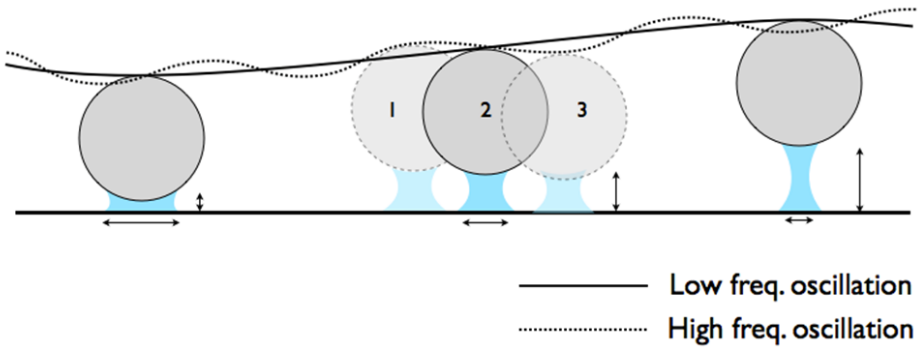

Figure 4.4: Schematic representation of the mechanisms for low and high frequency oscillations when contact between the tip (schematized as a sphere) and the surface is mediated by a liquid meniscus. Low frequency oscillations are caused by a deformation of the liquid drop as a whole. High frequency oscillations are due to a relative motion between tip and liquid, as represented in the sequence numbered 1, 2, 3. Note that the high frequency oscillations take place around an average constant tip height due to the much longer period of the low frequency oscillations.

counteracts the elastic forces of the cantilever (by the formation of liquid necks or menisci) and let the cantilever oscillate around the equilibrium position due to the thermal excitation. Since these attractive forces decrease further away from the surface, the negative contact stiffness results, similar to the case of the attractive part of the van der Waals interaction potential.

In all wavelet spectra shown in figure 4.3 the relative amplitudes (coded in a color scale) of the low frequency oscillations at 1-3 kHz are larger with respect to the higher frequency oscillations at 8.2 kHz. This suggest to explain the low frequency resonance as the motion of the tip and the condensed liquid drop as a whole (see figure 4.4), essentially due to the elastic deformation of the drop pulling the tip along. The initial deformation of the drop, with relatively large oscillations, is initiated by the impact of the tip. At the same time, the frequency resonance at 8.2 kHz is associated with the motion of the tip relative to the water condensate, having smaller amplitude. All the oscillations are sustained by the thermal motion of the cantilever.

The tip motion is composed by the sum of the oscillations produced by these independent mechanisms, accounting for the frequency-dependent

stiffness (drop deformation and relative motion). The resulting tip motion is a slow oscillation modulated by a faster one with the period ratio is approximately equal to 8:1 (see figure 4.4).

From the boundary conditions (equation 4.1) it is possible to deduce that the contact stiffness associated to the downshifting of the first mode resonance to 1-3 kHz is around $-0.99k$, as shown in figure 4.2b (exactly at $-k$ the frequency should be zero and the tip is in static neutral equilibrium). By summing the cantilever stiffness ($+k$) and the negative contact stiffness ($-0.99k$), as springs in parallel acting on the tip, a very small positive effective spring ($0.01k$) results, justifying the slow frequency oscillations. Analogously, the frequency resonance at 8.2 kHz is associated with the negative contact stiffness of $-0.6k$.

The presence of the resonance higher than f_1 in HOPG (and its absence in Si and PET), is attributed to the different wettability of the surfaces. The more hydrophilic nature of the Si and PET surfaces implies that water molecules are strongly bound to the surface and thus constitute a water film on which the tip lands after JTC. Instead, on the hydrophobic HOPG surface exposed to ambient air, there is a low probability of water condensation, resulting in the tip-sample contact mediated to a higher degree by short-range, Hertz-like forces, resulting in the positive contact stiffness. The tip proximity is favored in hydrophobic surfaces and prevented in hydrophilic surfaces due to the presence of the water film. The intermittent interactions with short-range repulsive forces are responsible of the first mode frequency upshift seen in HOPG (figure 4.3a,b).

To provide direct evidence of the different surface properties after JTC, the Boltzmann distribution sampled by the Brownian motion of the cantilever tip for each surface is reconstructed. From the Boltzmann distribution the associated potentials are derived [113,141]. The total tip potential (V_{tot}) is the sum of two contributions, the elastic potential of the cantilever ($V_{elastic}$) and the tip-sample contact potential (V_{ts})

$$V_{tot} = V_{elastic} + V_{ts}$$

Figure 4.5 shows the reconstructed potentials for HOPG, Si and PET. The red dots represents the total potential of the interacting tip after JTC (V_{tot}), obtained by detrending the contact line of the force curve and filtering out the high-order modes. These potentials are reconstructed from the low frequency parts (below 32 kHz) of the cantilever spectra. The

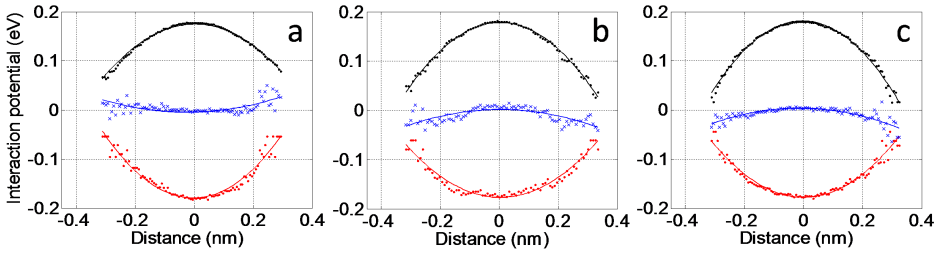

Figure 4.5: Potential energy of the tip retrieved from the Boltzmann distribution for (a) HOPG, (b) Si, (c) PET. In each graph is shown the negative of the free cantilever tip potential (black dots), total interacting potential after the jump-to-contact transition (red dots) and effective contact potential of the tip (blue crosses) obtained by subtracting the free potential from the total interacting potential. The continuous lines are parabolic fits to the data.

black dots represents the negative of the elastic potential of the free cantilever ($-V_{elastic}$), after filtering out the contribution of the higher-order modes as done for the interacting cantilever. The blue crosses show the effective contact potential in which the tip moves after JTC obtained by removing the contribution of the elastic potential from the total potential of the interacting cantilever.

It is important to note that the second derivative of the effective potential in HOPG has a different sign with respect to those in Si and PET. The concave upward (i.e. the second derivative is positive) of the effective potential in HOPG (figure 4.5a, blue line) means that the potential well of the interacting cantilever is narrower than the free potential well. A narrower potential imply a higher contact stiffness

$$k^* = -\partial^2 V_{ts}/\partial z^2$$

and a higher oscillation frequency

$$\omega \propto \sqrt{|\partial^2 V_{ts}/\partial z^2|}$$

confirming the conclusions obtained from the cantilever spectrum. The concave downward (i.e. the second derivative is negative) of the effective potential in Si and PET (figure 4.5b,c, blue lines) imply a potential well of the interacting cantilever wider that the free potential. This demonstrates a lower contact stiffness and a lower oscillations frequency, confirming the previous analysis.

4.5 Conclusions

In this chapter has been demonstrated how WT can be extremely useful when applied to the analysis of rapidly varying and non-stationary signals, like tip impacts on various kind of substrates. In particular, WT allows the analysis and characterization of temporal traces obtained during the JTC transition avoiding interruptions and averaging. Consequently it is possible to evidence the long (before JTC) and short (after JTC) range forces simultaneously.

WT analysis captures spectral features presented in cantilever oscillations that could not be evidenced using FT. The WT technique bears great potentials also in other research fields where transient signals are studied, for example in nanoscale thermomechanics [142], nanoacoustic devices [143] and in the investigation of nanostructures produced by laser ablation [144].

CHAPTER 5

Wavelet transform analysis of single-impact cantilever dynamics

5.1 Introduction

Usually the interaction of the tip with the surface, and hence the tip-sample forces, is disclosed by the modification of the average value of the varying cantilever parameters. The amplitude, frequency or phase shift is calculated over many oscillation cycles [2,3,38].

The possibility to capture information from single-event interactions event is not usually considered. Single-event interactions are basically of the impact kind (as the jump-to-contact transition), with the simultaneous excitation of many cantilever eigenmodes and/or harmonics and in this case, the tip-sample mutual influence reaches the regime where the interaction is limited to few oscillation cycles of the relevant cantilever eigenmodes. To study the few cycles regime, it is mandatory to provide analysis techniques that are able to characterize all the simultaneously excited cantilever oscillation frequencies at once and without averaging to retrieve quantitative information on materials properties such as the elastic constants and the sample chemical environment, with lateral resolution in the nanometer range. In addition, the few cycles regime opens the investigation of single events or interactions with samples that get destroyed or damaged after a single interaction with the cantilever tip.

Another fundamental aspect of the tip-sample interaction which allows to quantify compositional contrast variations at the nanoscale is the energy dissipation [12] since the applied forces and the energy delivered to the sample are relevant for the imaging and manipulation of soft materials in a variety of environments [145]. The study of the nanomechanical properties of the cell, the development of sensitive nanomechanical

devices, the characterization of mobile nanoparticles are all tasks that require a control of the force and energy involved in the tip-sample interactions [146].

In this chapter the method to analyze the dynamic of the thermally excited flexural modes of the cantilever during force spectroscopy measurement, in particular, the dynamics of the flexural modes of the cantilever when its tip is excited by a single impact on the sample surface is introduced.

The signal analysis is based on the simultaneous application of the continuous and cross-correlation wavelet transforms (see section 2.3). The results are model independent and based on the observation of the evolution of the spectra of the flexural modes during the JTC transition.

This approach gives possibility to reconstruct the tip dynamics in time-frequency space and to access the dissipated energy per cycle of each excited during the jump-to-contact transition flexural mode. Furthermore the instantaneous displacement, velocity and acceleration of the cantilever interacting tip are reconstructed.

The possibility of analyzing the responses of the cantilever caused by each mode participating in a few cycles interaction during an impulsive tip-sample interaction will be useful in many research aspects. The reconstruction of the complete evolution of the interaction force between the tip and the sample surface during a single interaction event pushes further the AFM possibilities.

5.2 Reconstruction the response signal of the interacting cantilever

The wavelet spectrum close-up of the impact region shows several contributions (see figure 5.1).

The spectrum of the free flexural modes excited by the Brownian motion of the cantilever is visible before the JTC point. A clear frequency bending of the first flexural mode (at 11.7 kHz, black dashed line) near the JTC is observed [125, 131]. The second flexural mode is visible as a dim trace at 80.5 kHz (white dashed line). In this case the frequency bending in the thermal trace before JTC is not visible, due to the increased stiffness of the second mode with respect to the first mode.

Upon impact, a strong excitation of the second mode at 65.3 kHz and

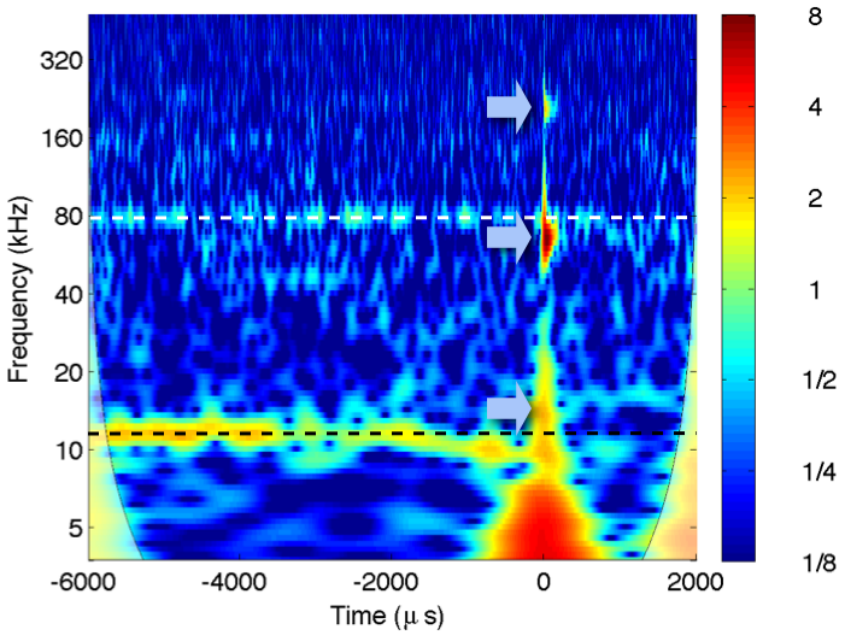

Figure 5.1: (Adapted from [33]) Wavelet spectrum of the signal before the jump-to-contact transition (at time zero). The thermal oscillations of the first (black dashed line, 11.7 kHz) and second (white dashed line, 80.5 kHz) flexural modes are visible at negative times. A clear frequency bending of the first mode is visible near the jump-to-contact transition. The arrows shows the modes excited by the tip impact on the sample during the jump-to-contact transition. Time zero corresponds to the JTC transition. Wavelet coefficients are coded in a color-scale. Both colors and frequencies are represented in octaves, i.e. base 2 logarithmic scales.

third mode at 207.5 kHz is clearly visible, accompanied by a spectral broadening of the first mode. It is interesting to note that the excited second mode has a downshifted frequency caused by the attractive forces. The amplitude of these contribution are proportional to the wavelet coefficients, coded in false colors. The excited modes have non-zero amplitude in a time window of approximately 200 μs. The broad region extending from 4 to 32 kHz is reminiscent of the first flexural mode, which is statically bent due to the attractive forces that are responsible of the JTC transition. As a consequence, in the 200 μs time window the cantilever dynamics is due exclusively to the second and third excited flexural modes. Note that in this time window the base of the cantilever travels

a small distance ($0.817\ nm/ms \times 200\ \mu s = 0.16\ nm$), allowing to neglect the effects of the piezo velocity on the cantilever dynamics.

Method to extract the frequency, amplitude and phase of the excited modes during the impact in order to capture the cantilever impact dynamics and reconstruct it with a simple model is presented below.

Each flexural mode is schematized as a damped harmonic oscillator, whose equation of motion is

$$\ddot{z} + \gamma\dot{z} + \omega_0^2 z = 0 \tag{5.1}$$

where z is the oscillation amplitude, γ is the damping coefficient, ω_0 the resonance frequency and dot $\dot{}$ represents the temporal derivative [9]. Considering for simplicity the initial conditions $z(0) = z_0$, $\dot{z}(0) = 0$ and assuming $\gamma \ll 1$, the solution is well approximated by an exponentially decaying amplitude oscillating at the resonance frequency:

$$z = z_0 e^{-\gamma t/2}\cos(\omega_0 t) = z_0 e^{-t/\tau}\cos(\omega_0 t) \tag{5.2}$$

where τ is the decay constant and $\gamma = 2/\tau$. The total signal $V(t)$ is a voltage proportional to the differential current coming from the top-bottom parts of the quadrant photodiode monitoring the beam deflection caused by the flexural modes. The temporal trace $V(t)$ captured by the beam deflection system is modeled by a sum of damped harmonic oscillators, representing the decaying modes,

$$V(t) = \sum_i V_i e^{-t/\tau_i}\cos(\omega_i t + \phi_i) \tag{5.3}$$

where V_i is the eigenmode voltage amplitude, τ_i is the eigenmode dacay constant, ω_i is the eigenmode angular frequency, $f_i = 2\pi/\omega_i$ is the eigenmode frequency, ϕ_i is the eigenmode phase, i is the eigenmode number.

The temporal trace can be reconstructed once the amplitude and phase of the oscillating component are known at a specific time. To measure the phases at a specific time, is used the wavelet cross-correlation with the reference sinc function (amplitude A=3, shaping factor a=1/3 μs), as explained before (see section 2.3.2). Since the static deflection is not important for the dynamics, the average deflection from the time window is subtracted, so that the relaxation oscillations are centered on the ordinate zero of the translated reference frame. Successively, the reference sinc function in this reference frame is translated and centered on the first

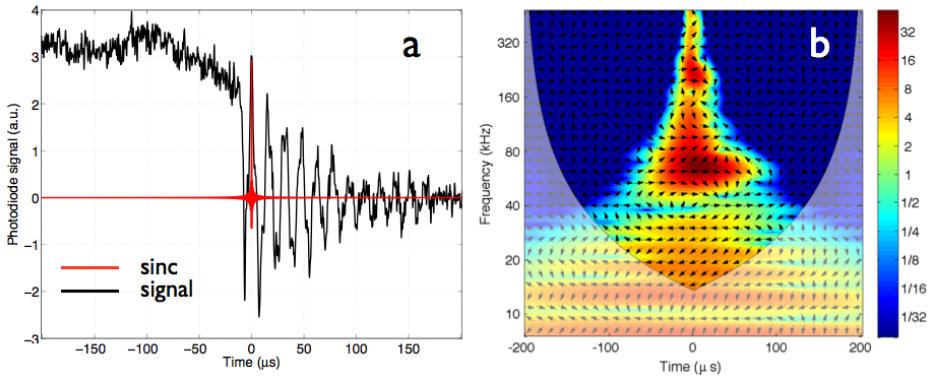

Figure 5.2: (Adapted from [33]) a) Relaxation oscillations of the signal after the jump-to-contact transition with the superposed sinc function. b) Wavelet cross-correlation of the traces shown in a. The amplitudes are coded in a color scale and show the common power between the temporal traces. Both colors and frequencies are represented in octaves, i.e. base 2 logarithmic scales. The black arrows slopes code the local phase-shift between the traces. The slope of the arrows arranged in a vertical row superposed on the wavelet spectra measures the local phase difference between the signal and the reference sinc function at time zero. The phase difference has been calculated through wavelet cross-correlation, as explained in the text. Arrow pointing right: $0°$; up: $-90°$; left: $180°$; down:$90°$. The areas, in which edge artifacts may distort the picture, are delimited by a lighter shade.

maximum, at the beginning of the impact time-window, and the relative phases between the signal and the reference sinc are measured.

Figure 5.2a shows the signal and the superposed sinc in the time domain. Since the sinc is constituted by a sum of cosines, the measured phases are referenced to cosines function whose origin are coincident with the sinc center. Figure 5.2b shows the cross-correlation wavelet analysis. A vertical cut of figure 5.2b allows to retrieve a bi-dimensional plot of the phase versus frequency.

In figure 5.3a is shown the wavelet spectrum with cuts at constant frequency (continuous red line and blue dashed line) and constant time (phase arrows lined up vertically)). Cuts at a constant time show the phase and amplitude evolution as a function of frequency (figure 5.3b,c). The values of interest is the amplitude and phase at the resonant frequencies of the excited modes (dots in figures 5.3b,c). Cuts at a constant

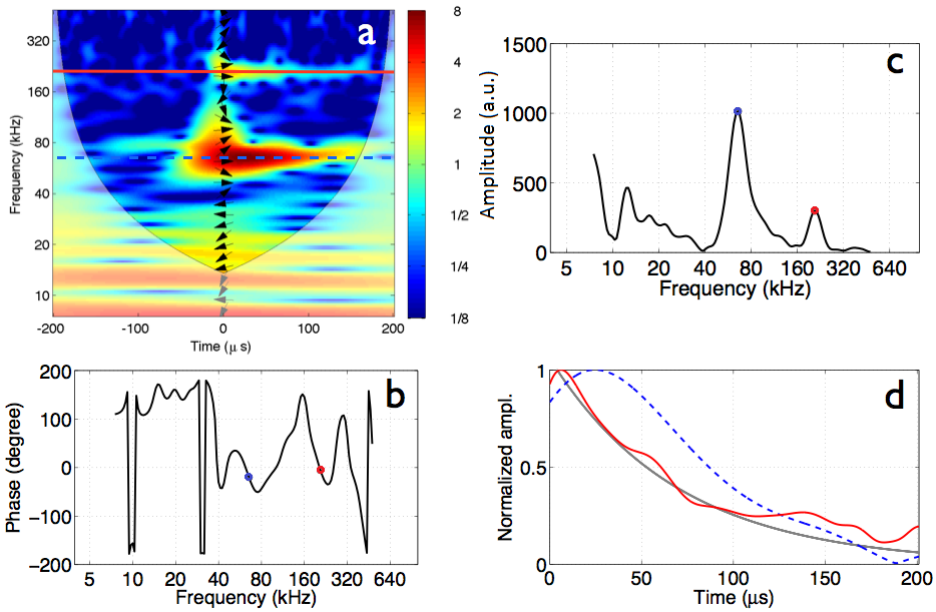

Figure 5.3: (Adapted from [33]) a) Wavelet spectrum of the signal close-up near the JTC transition. The transiently excited modes are evidenced by the blue dashed line (second mode) and continuous red line (third mode). Wavelet coefficients are coded in a color-scale. Both colors and frequencies are represented in octaves, i.e. base 2 logarithmic scales. The black arrows slopes code the local phase-shift between the traces. The slope of the arrows arranged in a vertical row superposed on the wavelet spectra measures the local phase difference between the signal and the reference sinc function at time zero. Arrow pointing right: $0°$; up: $-90°$; left: $180°$; down: $90°$. b) Phase-shift between the signal and the reference sinc as a function of frequency, at time zero. This curve is sampled and represented by the vertical line of black arrows in a. The dots are the phase values at the excited resonant frequencies. c) Amplitude profile as a function of frequency at time zero. The dots are the amplitude values at the excited resonant frequencies. d) Normalized amplitude profile as a function of time at the resonant frequencies of the second (blue dashed line) and third (continuous red line) modes. The continuous light gray line is an exponential decay with the decay constant of 70 μs for comparison.

frequency (figure 5.3d) show that the time decay of both modes can be approximated by decaying exponential function with the decay constant τ =70 μs (light grey line). The ratios of the amplitudes of the excited modes to the total initial amplitude (normalized to 1) are 0.77 and 0.23,

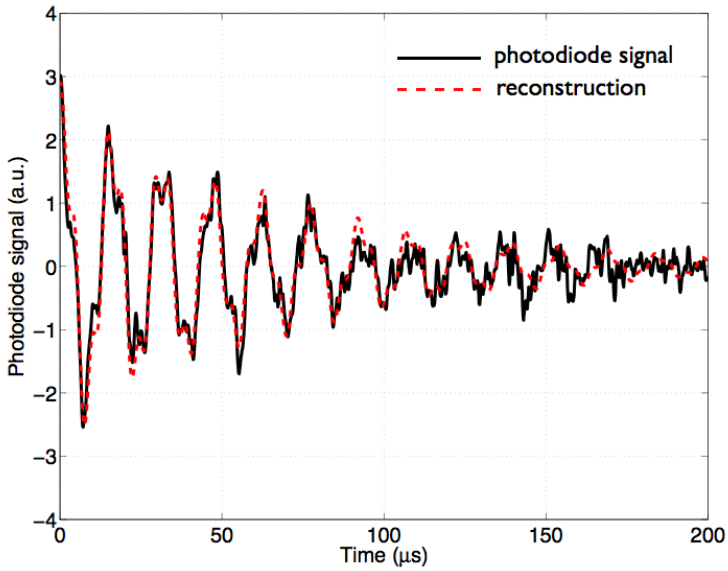

Figure 5.4: (Adapted from [33]) Reconstructed signal from equation 5.3 superposed on the relaxation oscillations after the jump-to-contact in 200 μs window.

their phases are -19.7° and -5.4° for the second and third modes respectively.

The phase angles and amplitudes, measured at the frequencies of the excited modes, constitute the inputs of the model. Inserting these values (i.e. initial amplitudes and phases) into equation 5.3, it is possible to reconstruct the photodiode signal as shown in figure 5.4. The reconstruction is not a fit, and only a multiplicative scale parameter is used to adapt the reconstructed photodiode signal to the experimental data.

From the reconstruction shown in figure 5.4, it is possible to calculate the effective displacement of the tip ($z(t)$) once the modal sensitivity of the beam deflection system is taken into account. In fact, since the optical beam deflection method actually measures the slope of the cantilever end, the same tip displacement generates a different photodiode signal depending on the cantilever mode that actuates it. The amplitude of the first mode (V_1) is calibrated with the standard static force spectroscopy method transforming the quadrant photodiode voltage into the tip displacement z_1 by using the calibration constant (InvOLS) c_1 (see section 3.2): $z_1(t) = V_1 c_1$. To retrieve the calibration constants for the higher modes the calculated optical sensitivity ratios for the beam deflection

Table 5.1: (Adapted from [33])Frequencies (f_i) and quality factors (Q_i) of the flexural modes measured in the 200 μs window during the cantilever impact. Frequencies are given in units of the first free flexural frequency. The theoretical free flexural frequencies ratios [4] and scaling for force constants (k_i) and optical sensibilities (σ_i) for each flexural mode [10] are shown for comparison.

Mode i	f_i/f_1 (exp.)	Q_i (exp.)	f_i/f_1 (theo.)	k_i/k_1 (theo.)	σ_i/σ_1 (theo.)
1	1	-	1	1	1
2	5.58	18	6.27	39.31	3.473
3	17.73	45	17.55	308	5.706

method need to be used [147].

The "real" displacement signal $z(t)$ is composed by the sum (superposition principle) of the total displacements of the cantilever $z_i(t)$ associated with the eigenmode number i

$$z(t) = \sum_i z_i(t) = \sum_i z_{0i} e^{-t/\tau_i} \cos(\omega_i t + \phi_i) \tag{5.4}$$

Each eigenmode displacement is given by

$$z_i(t) = z_{0i} e^{-t/\tau_i} \cos(\omega_i t + \phi_i)$$

where $z_{0i} = V_i c_1/\sigma_i$ is the amplitudes of the tip displacement in nm obtained from the voltage signal V_i through the calibration constant of the first mode c_1 and the parameter σ_i that takes into account the higher optical sensibility of the higher mode (see table 5.1).

In present case the photodiode signal is composed by the superposition of two modes. In figure 5.5a the tip trajectory is reconstructed using equation 5.4 (equation parameters are reported in table 5.2).

From the tip trajectory, all the quantities relevant to the tip motion can be calculated: velocity, force and force gradients.

Table 5.2: (Adapted from [33])Measured parameters used for the tip trajectory reconstruction in equation 5.4.

Mode i	f_i (kHz)	τ_i (μs)	ϕ_i (deg)	z_{0i} (nm)
2	65,3	70	-5.4	0.66
3	207,5	70	-19.7	0.12

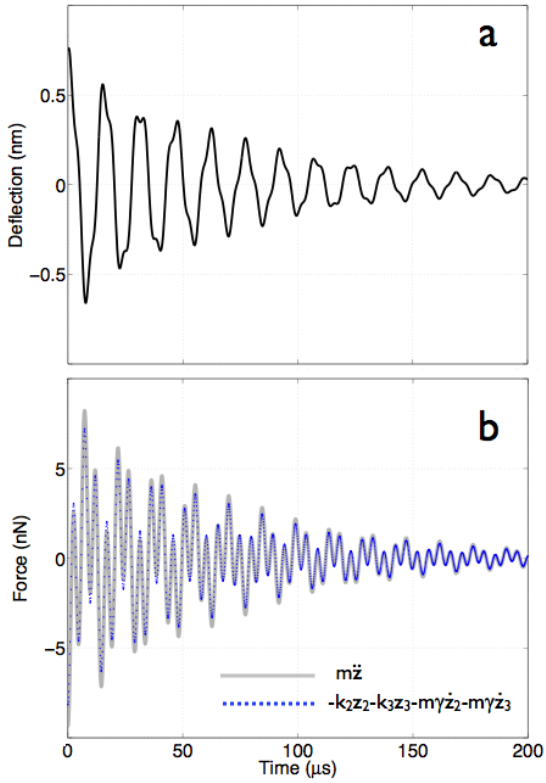

Figure 5.5: (Adapted from [33]) a) Instantaneous tip deflection. b) Instantaneous total force acting on the cantilever tip. The light gray line is obtained from the tip acceleration times the effective mass. The dotted blue line is obtained by summing the elastic and viscous forces for each mode.

In figure 5.5b the instantaneous total force acting on the tip (F_{tot}) is calculated computing the acceleration $\ddot{z}$ [148] from the displacement in equation 5.4 and considering the cantilever equivalent mass $m = m_{eq} = m_c/4$, which is constant regardless of the eigenmode, as discussed in [137]

$$F_{tot} = m\ddot{z} \tag{5.5}$$

The quality factors of two eigenmodes (see table 5.1) contributing to the tip total displacement are calculated as

$$Q_i = 2\pi f_i/\gamma$$

where γ is the friction coefficient, connected with the decay constant by

$\gamma = 2/\tau$.

The quality factor ratio between the eigenmodes of a damped cantilever scales as the frequencies [10], so the ratio $Q_3/Q_2 = 2.8$ is expected and 2.5 is measured.

It is important to note that the cantilever is not free, but nearly behaves as a free cantilever with modified damping factors. The external forces occurring during the relaxation oscillations of the cantilever after the JTC impact behave as an effective viscous force with the friction coefficient γ. Their influence manifests in the heavily reduced quality factors measured in this case with respect to the free cantilever (e.g. see [149]). The fact that the quality factor scaling is approximately respected is an indication that the viscous damping mechanism implicitly assumed in modeling the cantilever as a sum of damped harmonic oscillators is a good approximation.

The instantaneous total force acting on the tip can be retrieved using the different route by summing the elastic and viscous forces acting on each mode of the cantilever

$$F_{tot} = -k_2 z_2 - k_3 z_3 - m\gamma v_2 - m\gamma v_3 \tag{5.6}$$

where k_2, k_3 are the force constants, z_2, z_3 are the deflections and v_2, v_3 are the velocities associated with the second and third modes of the cantilever respectively.

In figure 5.5b the total force obtained from the tip acceleration and that one obtained from the elastic and viscous contribution are compared. The fact that the forces are nearly coincident constitutes a good reliability test for the present analysis. Note, that since the quality factors are relatively high, the viscous force is small in comparison to the elastic contribution.

From the analysis above deduced that the tip dynamics in 200 μs window after JTC is composed by the sum of two decaying modes that resemble two mass-spring systems with viscous damping. It is important to note that the modal structure of the cantilever is not that of the pinned cantilever, but that of the damped cantilever with the blocked first eigenmode.

In the experiment has been used the silicon tip on HOPG sample. Considering that the maximum total displacement during the mode excitation after the impact is of the order of the lattice spacing of silicon (5.43 Å) or 1.5 times of the distance between the graphite planes (3.35 Å) or four times of the distance between the hydrogen atoms in water (1.51 Å), that could

absorb on the oxidized silicon tip or (less probably) on the hydrophobic graphite surface, could be concluded that the relaxation oscillations after the tip impact can be attributed to a combination of local deformation of the materials and/or water capillary forces.

5.3 Modal energy dissipation due to the tip-sample interaction

As has been shown in preceding section 5.2, the following steps, synthesized in figure 5.6, allow to reconstruct the evolution of a multi-mode excitation of the cantilever, after the jump-to-contact transition. 1) Single out the time period of interest, i.e. the neighborhood of the impact moment (figure 5.6b). 2) Take WT of the signal and individuate the excited modes contributing to the dynamics (figure 5.6c). 3) Each flexural mode ia schematized as a damped harmonic oscillator (DHO) (see equation 5.1), then the solution is well approximated by an exponentially decaying amplitude oscillating at the resonance frequency (see equation 5.2). 4) Retrieve the parameters of each DHO through the WT and XWT analyzes (figure 5.6c). 5) Reconstruct the cantilever signal as a sum of DHO (figure 5.6d).

In particular the WT allows to retrieve, for each mode, the amplitude, decay constant and frequency. Further, the XWT (see section 2.3.2) retrieves the phase relative to the sinc function at a specific time, usually at the beginning of the time period of interest. With this information, following the superposition principle, it is possible to sum the contributions of the DHO and reconstruct the signal obtained from the beam deflection apparatus measuring the cantilever dynamics (see section 5.2).

The first free flexural mode does not contribute to the dynamics because it remains statically bent towards the surface after the impact due to the jump-to-contact transition. The excited modes have frequencies that scale nearly as the second and third free flexural modes (see table 5.3) and contribute to the relaxation oscillations that are seen in figure 5.6b. For these reasons the excited modes will be labeled as the second and third modes.

The reconstruction of the photodiode signal does not yet represent the effective displacement of the cantilever tip due to the characteristics of the beam deflection apparatus, which is used in the experiments.

Usually the deflection signal measured from the cantilever does not

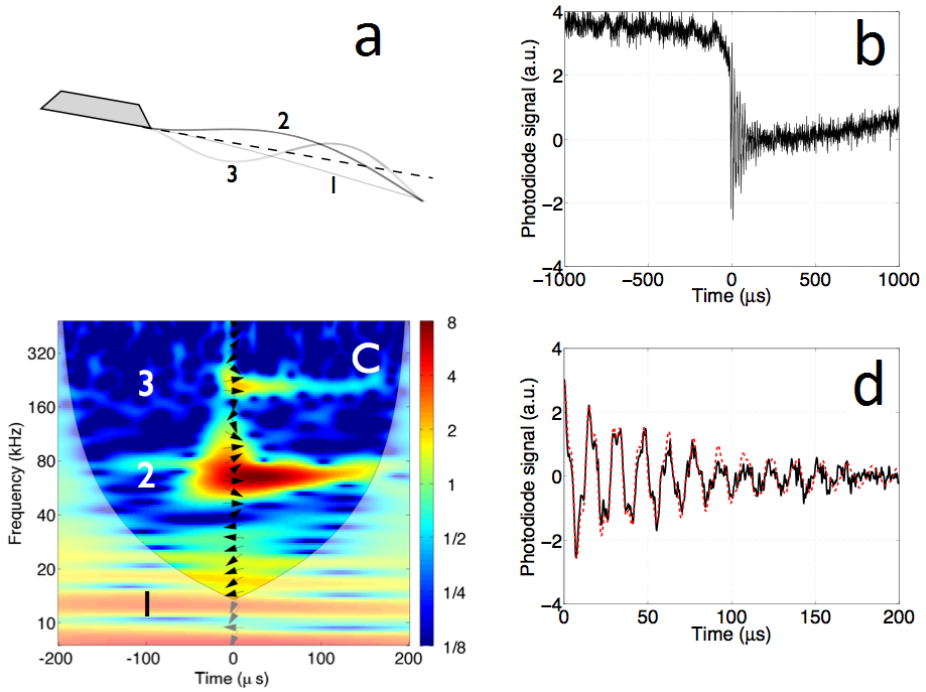

Figure 5.6: (Adapted from [34]) Synthesis of the wavelet retrieval method. a) Schematic diagram of the modal shapes of the cantilever flexural modes. b) The time evolution of the relaxation oscillations after the cantilever jump-to-contact transition. c) The wavelet analysis of the relaxation oscillations. The numbers refers to the excited flexural modes of the cantilever, schematized in a. Note that the fundamental mode does not oscillate because it remains statically bent after the jump-to-contact. Wavelet coefficients are coded in a color-scale. Both colors and frequencies are represented in octaves, i.e. base 2 logarithmic scales. The slope of the arrows arranged in a vertical row superposed on the wavelet spectra measures the local phase difference between the signal and the reference sinc function at time zero. The phase difference has been calculated through wavelet cross-correlation, as explained in the text. Arrow pointing right: $0°$; up: $-90°$; left: $180°$; down: $90°$. The areas, in which edge artifacts may distort the picture, are delimited by a lighter shade. d) Reconstruction (red-dotted line) of the relaxation oscillations (continuous black line) obtained by the superposition of damped harmonic oscillators as detailed in the text.

relate directly to the tip displacement, this is the case only when calibrated interferometers are used. Other techniques monitor the velocity through the Doppler velocimeter or the bending of the cantilever when using the

Table 5.3: (Adapted from [34])Theoretical [4] and experimental free flexural frequencies of the excited modes in units of the first free flexural frequency and the theoretical scaling of the force constants (k_i) for each flexural mode [10].

Mode i	f_i/f_1 (theo.)	f_i/f_1 (exp.)	k_i/k_1 (theo.)
1	1	1	1
2	6.27	5.58	39.3
3	17.55	17.73	308

popular beam deflection method. It is necessary to relate the signal measured by the instrument (and reconstructed by the DHO) to the real tip deflection. In the beam deflection method used in this experiment, the measured signal is proportional to the cantilever bending at the position of the laser spot, usually at the end of the cantilever. While the InvOLS of the first free flexural mode, which relates the bending of the cantilever to the deflection of the tip, is calibrated by using the static force curve, those of the higher modes are not. For the same tip deflection, the higher the mode the higher the bending of the cantilever end. This means that the InvOLS of the first free flexural mode must be corrected to relate the measured bending that is caused by higher modes to the corresponding tip deflections. This is done by means of the optical sensitivities σ_i reported in table 5.4.

This procedure allows to obtain the parameters of the DHO needed to reconstruct the cantilever deflection mode by mode. The parameters that are used to reconstruct the second and third DHO mode dynamics, and hence the total tip deflection, are reported in table 5.4. Once the deflections of the second and third eigenmodes have been quantified, it is possible to access the velocity and acceleration of the tip caused by each flexural mode.

Table 5.4: (Adapted from [34]) Optical sensibilities σ_i and damped harmonic oscillator parameters used for the tip trajectory reconstruction.

Mode i	σ_i (theo.)	z_{0i} (nm)	τ_i (μs)	f_i (kHz)	ϕ_i (deg)
1	1	-	-	-	-
2	3.4731	0.66	70	65.3	-5.4
3	5.706	0.12	70	207.5	-19.7

The description of the dynamics by using uncoupled DHO during the JTC is justified, because from the experiment no hints of a nonlinear coupling between the modes are observed, and two uncoupled DHO are sufficient to reconstruct the detail of the experimental trace. In addition, and contrary to intuition, the second and third modes are not contact modes. This is proved by their frequency scaling, which is similar to that of the free flexural modes and differs considerably from that of the pinned cantilever flexural modes (see tables 4.1,5.3).

The energy balance of each decaying mode obtained from equation 5.1 in the time window $0 < t < \tau = 200\mu s$ (see figure 5.6) can be written as

$$E_{\gamma_i} = E_{b_i} \tag{5.7}$$

$$E_{\gamma_i} = \int_0^\tau m_{eq}\gamma_i \, v_i^2 dt$$

$$E_{b_i} = \Delta K_i + \Delta U_i$$

$$\Delta K_i = \frac{1}{2} m_{eq}(v_i(0)^2 - v_i(\tau)^2)$$

$$\Delta U_i = \frac{1}{2} k_i(z_i(0)^2 - z_i(\tau)^2)$$

where E_{γ_i} is the term that depends on the time-integrated dissipative power, E_{b_i} is the term that depends on the balance of the potential and kinetic energy, ΔK_i is the variation of kinetic energy, ΔU_i is the variation of elastic potential energy, t is the integration time, i is the index of the eigenmode. The dissipative constants γ_i are parameters that take into account the influence of the external environment, which is modeled as a viscous force. Note, that the elastic force of the cantilever is a conservative force that does not contribute to the dissipation. Dissipation is intrinsically difficult to explain microscopically in situations where the ambient environment is complex (presence of gas molecules, water layers, etc.) but interesting since it potentially carries information about the tip-sample interactions. Since the coefficients γ_i and k_i are measured/estimated independently, the energy balance described in equation 5.7 is a test of the internal consistency of the model.

The elastic constants of the higher modes are equal to the values calculated by the scaling from beam theory (see table 5.3). The equivalent mass (m_{eq}) for the rectangular cantilever is the same for all modes and

Table 5.5: (Adapted from [34]) Total dissipated energy calculated by a balance of potential and kinetic energy (E_b) and by integrating the dissipative forces (E_γ). Quality factor is derived as $Q_i = 2\pi f_i/\gamma_i$, where the damping coefficient $\gamma_i = 2/\tau_i$ (see table 5.4). Elastic constant is derived from the theoretical scaling (k_i) and from the oscillator parameters ($m_c/4\omega_{0i}^2$)

Mode i	E_{b_i} (eV)	E_{γ_i} (eV)	γ_i ($10^4 s^{-1}$)	Q_i (exp.)	k_i (N/m)	$m_c/4\omega_{0i}^2$ (N/m)
2	5.97	5.97	2.85	14	5.9	4.4
3	2.00	1.98	2.85	45	46.2	44.5

equal to one quarter of the cantilever mass (m_c) [137]. Calculating the energy balance using these parameters in equation 5.7 shows the emerging of a discrepancy in the energy balance of the second mode. The variation of total energy $E_{b_2} = 7.8\ eV$ does not match the integrated dissipation $E_{\gamma_2} = 6\ eV$.

Another way to assess the consistency of the model is to use the total force test, which means to compare the total forces acting on the tip calculated via the inertial mass (see equation 5.5) with the total forces calculated via stiffness and dissipative forces (see equation 5.6). In this case a good match is obtained (see section 5.2). This means that even if the level of agreement in the total force test appears to be satisfactory, the more stringent energy balance test singles out the discrepancy.

The reason of the discrepancy in the energy balance is attributed to a different degree of interaction of the higher cantilever eigenmodes with the surface forces. The force gradient at the sample surface modifies the equivalent stiffness of the interacting cantilever by shifting the resonance frequency to the lower values for the attractive interactions [2]. In this case the effective stiffness of the cantilever is not that of the free cantilever, as implicitly assumed using the stiffness scaling from the beam theory.

The elastic constant of each mode (k_i) is connected to the mode resonant frequency (ω_{0i}) as [137]

$$k_i = \frac{m_c}{4}\omega_{0i}^2$$

where i is the mode index. Since in this case the resonant frequency seen in the wavelet transform (figure 5.6c) is that of the interacting cantilever, one would expect that the cantilever stiffness calculated by using

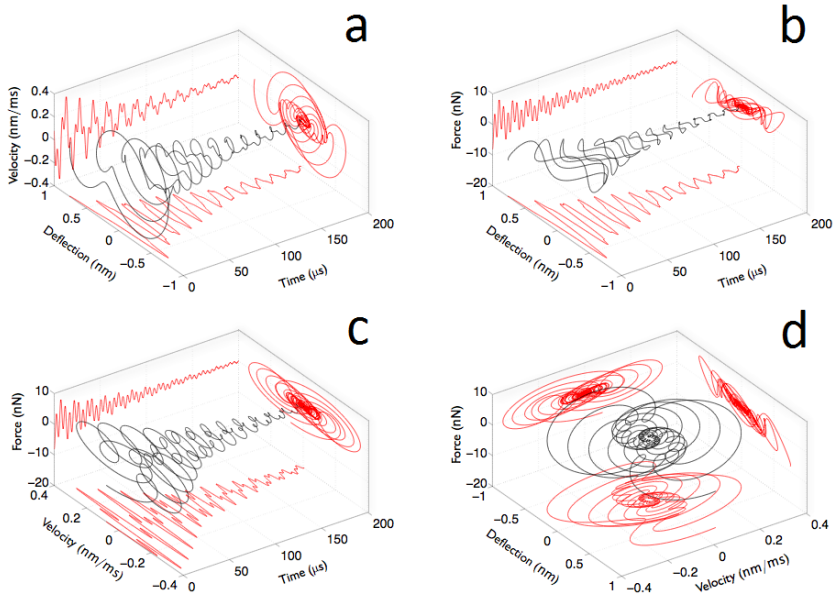

Figure 5.7: (Adapted from [34]) 3D representation of the main observables describing the cantilever tip dynamics during the impact following the jump-to-contact transition.

the equivalent mass and the resonant frequency should incorporate the effects of the surface force gradients. In the present case, the scaling of the elastic constant from the beam theory is respected with a good approximation for the third mode but not for the second (table 5.5).

In order to obtain a good matching with the integrated dissipation, the equivalent stiffness of the second mode has to be taken equal to $m_c/4\omega_{02}^2$. The overall quality of the match F_m vs F_γ improves and a very good agreement of the variation of the total energy (E_{b_i}) and integrated dissipation (E_{γ_i}) for both modes is obtained (table 5.5).

Having a general consistency regarding the energy conservation, the correct estimation of the dissipated energy per cycle in each eigenmode is obtained as the difference between the maximum elastic energy stored in successive cycles (figure 5.8).

As expected the energy dissipated per cycle in both eigenmodes contributing to the cantilever dynamics decays exponentially. The quantifi-

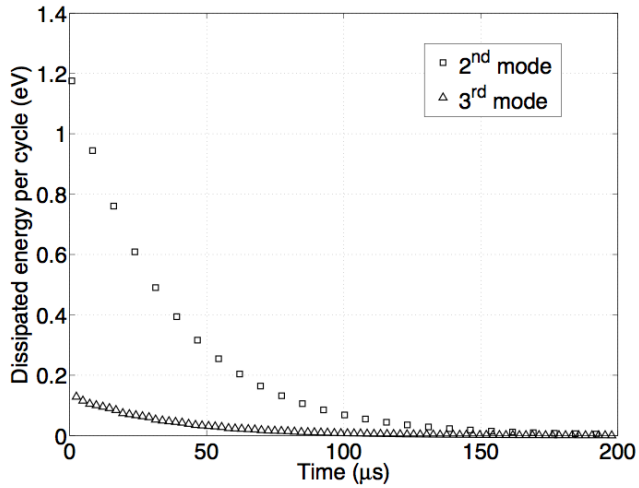

Figure 5.8: (Adapted from [34])Dissipated energy per cycle in each mode contributing to the dynamics described in figure 5.7

cation of the dissipation per mode evidenced a rather gentle interaction, with the total energy released from the tip of the order of 8 eV during the whole impact, considering that typical tapping mode interactions release energies per one tap on the order of several tens of eV [150]. Moreover, the maximum energy released in a single cycle during the impact does not exceed 1.2 eV for the second mode and 0.13 eV for the third mode. The energy is released by eigenmodes characterized by the different oscillations frequencies, thus opening the possibility to resonant energy transfer to samples or (nano)structures endowed with mechanical resonances at the eigenmode frequencies.

Figure 5.7 shows the evolution of the instantaneous deflection (z), force (F) and velocity (v) as a function of time in various 3D representations and a comprehensive representation of the phase-space of the motion. The spiraling trajectories are connected and they are a visual representation of the dissipated energy. Figure 5.7a is a representation of the displacement-velocity phase-space evolving in time. Figure 5.7b,c are connected to the total instantaneous work ($F \cdot zdt$) and power ($F \cdot vdt$), respectively, done on the tip during its displacement dz from time t to time $t + dt$. Figure 5.7d is a representation of the phase-space parameters F, v, z.

5.4 Conclusions

Using the wavelet transform it is possible to analyze the spectral evolution of the modes of the cantilever interacting impulsively with the sample surface. The excitation of multiple flexural modes is evidenced and the instantaneous amplitude and phase evolution of the oscillations of the cantilever after the single tip-sample impact are extracted from the experimental data at all frequencies simultaneously using the wavelet analysis. Since the temporal development of the damped oscillating modes evolves continuously in time, i.e. the coherence time of the mode is longer than the observation period, knowing the amplitude and phase at a specific time allows to reconstruct the photodiode signal from the beam deflection apparatus. Successively, correcting for the modal sensitivity of the beam deflection system, the tip trajectory is obtained and the instantaneous total force acting on the tip during the single impact is reconstructed. The phases of the modes are assessed by cross-correlating their wavelets transforms with the reference sinc function, acting as a phase reference for the signal. The cross-correlation wavelet analysis allows retrieving the energy dissipation, displacement, velocity and acceleration of the tip for each flexural eigenmode upon impact simultaneously.

The techniques outlined in this chapter will be useful to characterize the mechanical contact properties of nanostructures produced by femtosecond laser ablation, to disentangle oscillatory modes probed by picosecond acoustics techniques [142] and to describe the compositional contrast of the sample at the nanometer scale through the dissipative interactions [151]. The present analysis will enlarge the space of parameters to be exploited for the sensing action.

This approach has general relevance for the development of an atomic force spectroscopy of single tip-sample interactions that develop in few oscillation cycles of the interacting cantilever eigenmodes and their harmonics.

Perspectives

The wavelet analysis has already been implemented in some applications in the field of AFM spectroscopy, however the full range of possibilities offered by the WT as a method of data processing is far from being fully developed yet. Up to recent times, the WT technique has been used in AFM principally to denoise images or extract data from noisy signals [152, 153].

The application of WT to extract information from dynamic AFM spectroscopy has been introduced only recently and it is an upcoming way to characterize surface material properties at the nanoscale. It has been demonstrated that WT allows to characterize long- and short-range forces as well as complex force dynamics with quantitative results. Nonlinear interactions are extremely sensitive to small changes in tip-sample interactions and WT is a useful tool to gain information from such nonlinear interactions [7, 30, 31, 139, 140, 154]. WT is able to follow the temporal evolution of nonlinearities in force curves [20, 22, 155] and furthermore gives the possibility to retrieve interaction forces [102].

In case of impacts (single or multiple) by the investigation of the cantilever signal spectrum around the impact region, information on the tip-sample interaction dynamics can be obtained. The type of material properties that WT could contribute to study and that is not readily measured by other methods depends on two characteristics of the wavelet analysis. First, WT allows to study the tip trajectory and the spectral content as a function of time for each mode separately. Second, WT can extract information without averaging. Having a model to represent the tip-sample

interaction as a function of time, it is foreseen that a fit of the theory, depending on a restricted set of parameters, to the experiments could bring new informations. For example, in viscoelastic materials, the elasticity parameters depends on how fast the deformation force is applied to the material. WT could be used to investigate these time-dependent material responses. In situations where an impact experiment cannot be repeated, WT provides a complete dynamical information that is not readily available through other methods. As an example, consider a tip-sample impact that destroys the sample. In this case all the information must be retrieved by a single force curve, without averaging.

XWT analysis has been employed only recently and it opens further perspectives for the application of WT in AFM measurements. This technique allows to determine the phase relationship between the driving force and the response of the cantilever [126, 156].

By using WT analysis it becomes possible to get a full picture of the temporal evolution of the amplitude and relative phase of each mode of the cantilever which gives information about mechanical contact properties of the surface. The values of the amplitude and the phase at a precise time allow to reconstruct the photodiode signal and the tip trajectory.

Few cycles tip-sample interactions reduce the acquisition time and allow for a multiparameter analysis. This will enlarge the physical information gained by the tip-sample interaction. The methodology presented here will be beneficial to other fields exploiting impulsive force phenomena.

The techniques outlined in this thesis will find applications in a variety of fields of interest for nanotechnology and with further work will ultimately provide information about the contact mechanical properties of the surface.

Bibliography

[1] G. Binnig, C. C. Quate, and C. Gerber. Atomic force microscope. *Phys. Rev. Lett.*, 56:930, 1986.

[2] S. Morita, R. Wiesendanger, and E. Meyer, editors. *Noncontact Atomic Force Microscopy*. Springer, Berlin, 2002.

[3] R. Garcia. *Amplitude modulation atomic force spectroscopy*. Wiley-VCH, first edition, 2010.

[4] H. J. Butt and M. Jaschke. Calculation of thermal noise in atomic force microscopy. *Nanotechnology*, 6:1, 1995.

[5] A. Roters and D. Johannsmann. Distance-dependent noise measurements in scanning force microscopy. *J. Phys.: Condens. Matter*, 8:7561, 1996.

[6] A. Roters, M. Gelbert, M. Schimmel, J. Rühe, and D. Johannsmann. Static and dynamic profiles of tethered polymer layers probed by analyzing the noise of an atomic force microscope. *Phys. Rev. B*, 56:3256, 1997.

[7] P. Vairac, B. Cretin, and A. J. Kulik. Towards dynamical force microscopy using optical probing of thermomechanical noise. *Appl. Phys. Lett.*, 83:3824, 2003.

[8] A. Gannepalli, A. Sebastian, J. Cleveland, and M. Salapaka. Thermally driven non-contact atomic force microscopy. *Appl. Phys. Lett.*, 87:111901, 2005.

[9] L. D. Landau and E. M. Lifshitz. *Mechanics*. Elsevier Butterworth-Heinemann, Oxford, third edition, 1976.

[10] R. Garcia and E. T. Herruzo. The emergence of multifrequency force microscopy. *Nature Nanotech.*, 7:217, 2012.

[11] J. R. Lozano and R. Garcia. Theory of multifrequency atomic force microscopy. *Phys. Rev. Lett.*, 100:076102, 2008.

[12] S. Jesse, S. V. Kalinin, R. Proksch, A. P. Baddorf, and B. J. Rodriguez. The band excitation method in scanning probe microscopy for rapid mapping of energy dissipation on the nanoscale. *Nanotechnology*, 18:435503, 2007.

[13] A. U. Kareem and S. D. Solares. Characterization of surface stiffness and probe–sample dissipation using the band excitation method of atomic force microscopy: a numerical analysis. *Nanotechnology*, 23:015706, 2012.

[14] N. F. Martinez, S. Patil, J. R. Lozano, and R. Garcia. Enhanced compositional sensitivity in atomic force microscopy by the excitation of the first two flexural modes. *Appl. Phys. Lett.*, 89:153115, 2006.

[15] N. F. Martinez, J. R. Lozano, E. T. Herruzo, F. Garcia, C. Richter, T. Sulzbach, and R. Garcia. Bimodal atomic force microscopy imaging of isolated antibodies in air and liquids. *Nanotechnology*, 19:384011, 2008.

[16] D. Ebeling and S. D. Solares. Bimodal atomic force microscopy driving the higher eigenmode in frequency-modulation mode: Implementation, advantages, disadvantages and comparison to the open-loop case. *Beilstein J. Nanotechnol.*, 4:198, 2013.

[17] A. Raman, S. Trigueros, A. Cartagena, A. P. Z. Stevenson, M. Susilo, E. Nauman, and S. A. Contera. Mapping nanomechanical properties of live cells using multiharmonic atomic force microscopy. *Nature Nanotech.*, 6:809, 2011.

[18] S. Crittenden, A. Raman, and R. Reifenberger. Probing attractive forces at the nanoscale using higher-harmonic dynamic force microscopy. *Phys. Rev. B*, 72:235422, 2005.

[19] J. Preiner, J. Tang, V. Pastushenko, and P. Hinterdorfer. Higher harmonic atomic force microscopy: imaging of biological membranes in liquid. *Phys. Rev. Lett.*, 99:046102, 2007.

[20] O. Sahin, S. Magonov, C. Su, C.F. Quate, and O. Solgaard. An afm tip designed to measure time-varying nanomechanical forces. *Nature Nanotechnology*, 2:507, 2007.

[21] S. D. Solares and H. Hölscher. Numerical analysis of dynamic force spectroscopy using the torsional harmonic cantilever. *Nanotechnology*, 21:075702, 2010.

[22] M. Stark, R. W. Stark, W. M. Heckl, and R. Guckenberger. Inverting dynamic force microscopy: from signals to time-resolved interaction forces. *PNAS*, 99:8473, 2002.

[23] R. W. Stark and W. M. Heckl. Higher harmonics imaging in tapping-mode atomic-force microscopy. *Rev. Sci. Instrum.*, 74:5111, 2003.

[24] R. W. Stark. Dynamics of repulsive dual-frequency atomic force microscopy. *Appl. Phys. Lett.*, 94:063109, 2009.

[25] R.W. Stark. Bistability, highter harmonics, and chaos in afm. *Materials today*, 13:24, 2010.

[26] V. L. Mironov. *Fundamentals of scanning probe microscopy*. The Russian Academy of Sciences, Nizhniy Novgorod Russia, 2004.

[27] D. Sarid. *Scanning Force Microscopy*. Oxford University Press, 1991.

[28] F. J. Giessibl. Advances in atomic force microscopy. *Rev. Mod. Phys.*, 75:949, 2003.

[29] R. Garcia and R. Perez. Dynamic afm methods. *Surf. Sci. Reports*, 47:197, 2002.

[30] P. M. Hoffmann, A. Oral, R. A. Grimble, H. Ö. Özer, S. Jeffery, and J. B. Petica. Direct measurement of interatomic force gradients using an ultra-low-amplitide atomic force microscope. *Proc. R. Soc. Lond. A*, 457:1161, 2001.

[31] N. Oyabu, P. Pou, Y. Sugimoto, P. Jelinek, M. Abe, S. Morita, R. Perez, and O. Custance. Single atomic contact adhesion and dissipation in dynamic force microscopy. *Phys. Rev. Lett.*, 96:106101, 2006.

[32] V. Pukhova, F. Banfi, and G. Ferrini. Transient eigenmodes analysis of single-impact cantilever dynamics combining fourier and wavelet transforms. *Nanotechnology*, 2015.

[33] V. Pukhova, F. Banfi, and G. Ferrini. Complex force dynamics in atomic force microscopy resolved by wavelet transforms. *Nanotechnology*, 24:505716, 2013.

[34] V. Pukhova, F. Banfi, and G. Ferrini. Energy dissipation in multifrequency atomic force microscopy. *Beilstein J. Nanotechnol.*, 5:494, 2014.

[35] Y. Martin, C. C. Williams, and H. K. Wickramasinghe. Atomic force microscope-force mapping and profiling on a sub 100-angstrom scale. *J. Appl. Phys.*, 61:4723, 1987.

[36] G. Meyer and N. M. Amer. Novel optical approach to atomic force microscopy. *Appl. Phys. Lett.*, 53:2400, 1988.

[37] T. Fukuma, J. I. Kilpatrick, and S. P. Jarvis. Phase modulation atomic force microscopy with true atomic resolution. *Rev. Sci. Instrum.*, 77:123703, 2006.

[38] S. Morita, F. J. Giessibl, and R. Wiesendanger, editors. *Noncontact Atomic Force Microscopy*, volume II. Springer, Berlin, 2009.

[39] T. R. Albrecht, P. Grütter, D. Horne, and D. Rugar. Frequency modulation detection using high-Q cantilevers for enhanced force microscope sensitivity. *J. Appl. Phys.*, page 668, 1991.

[40] U. Dürig, H. R. Steinauer, and N. Blanc. Dynamic force microscopy by means of the phase-controlled oscillator method. *J. Appl. Phys.*, 82:3641, 1997.

[41] F. J. Giessibl. Afm's path to atomic resolution. *Materials Today*, 8:32, 2005.

[42] T. Fukuma, K. Kobayashi, K. Matsushide, and H. Yamada. True atomic resolution in liquid by fm-afm. *Appl. Phys. Lett.*, 87:034101, 2005.

[43] P. Parot. Past, present and future of afm in life sciences and medicine. *J. Mol. Recognit.*, 20:418, 2007.

[44] R. Garcia, R. Magerle, and R. Perez. Nanoscale compositional mapping with gentle forces. *Nat. Mater.*, 6:405, 2007.

[45] Y. Gan. Atomic and subnanometer resolution in ambient conditions by afm. *Surf. Sci. Rep.*, 64:99, 2009.

[46] H. Yamada. Molecular resolution imaging of protein molecules in liquid using fm-afm. *Appl. Phys. Lett.*, 2:095007, 2009.

[47] M. J. Higgins, R. Proksch, J. E. Sader, M. Polcik, S. Mc Endoo, J. P. Cleveland, and S. P. Jarvis. Noninvasive determination of optical lever sensitivity in atomic force microscopy in atomic force microscopy. *Rev. Sci. Instrum.*, 77:013701, 2006.

[48] R. Proksch. Multifrequency, repulsive-mode amplitude-modulated atomic force microscopy. *Appl. Phys. Lett.*, 89:113121, 2006.

[49] R.W. Stark, N. Naujoks, and A.Stemmer. Multifrequency electrostatic force microscopy in the repulsive regime. *Nanotechnology*, 18:065502, 2007.

[50] A. San Paulo, J.P. Black, R.M. White, and J. Bokor. Detection of nanomechanical vibrations by dynamic force microscopy in higher cantilever eigenmodes. *Appl. Phys. Lett.*, 91:053116, 2007.

[51] S. Patil, N. F. Martinez, J. R. Lozano, and R. Garcia. Force microscopy imaging of individual protein molecules with sub-pico newton force sensitivity. *J. Mol. Recognit.*, 20:516, 2007.

[52] S. Basak and A. Raman. Dynamics of tapping mode atomic force microscopy in liquids: theory and experiments. *Appl. Phys. Lett.*, 91:064107, 2007.

[53] R. W. Stark and W. M. Heckl. Fourier transformed atomic force microscopy: tapping mode atomic force microscopy beyond the hookian approximation. *Surf. Sci.*, 457:219, 2000.

[54] T. R. Rodriguez and R. Garcia. Compositional mapping of surfaces in atomic force microscopy by excitation of the second normal mode of the microcantilever. *Appl. Phys. Lett*, 84:449, 2004.

[55] N. Balke, S. Jesse, A. N. Morozovska, E. Eliseev, D. W. Chung, Y. Kim, L. Adamczyk, R. E. García, N. Dudney, and S. V. Kalinin. Nanoscale mapping of ion diffusion in a lithium-ion battery cathode. *Nature Nanotech.*, 5:749, 2010.

[56] M. Stark, R.W. Stark, W. Heckl, and R. Guckenberger. Spectroscopy of the anharmonic cantilever oscillations in tapping-mode atomic force microscopy. *Appl. Phys. Lett.*, 77:3293, 2000.

[57] B. J. Rodriguez and R. Garcia. Tip motion in amplitude modulation (tapping-mode) afm: comparison between continuous and point-mass models. *Appl. Phys. Lett*, 80:1646, 2002.

[58] O. Sahin, G. Yaralioglu, R. Grow, S.F. Zappe, A. Atalar, C. Quate, and O. Solgaard. High-resolution imaging of elastic properties using harmonic cantilevers. *Sen. and Act. A*, 114:183, 2004.

[59] M. Balantekin and A. Atalar. Enhanced higher-harmonic imaging in tapping-mode atomic force microscopy. *Appl. Phys. Lett.*, 87:243513, 2005.

[60] Y. Sugimoto, S. Innami, M. Abe, O. Custance, and S. Morita. Dynamic force spectroscopy using cantilever higher flexural modes. *Appl. Phys. Lett.*, 91:093120, 2007.

[61] H. Ueyama, Y. Sugawara, and S. Morita. Stable operation mode for dynamic noncontact atomic force microscopy. *Appl. Phys. A*, 66:S295, 1998.

[62] L. Nony, A. Baratoff, D. Schär, O. Pfeiffer, A. Wetzel, and E. Meyer. Noncontact atomic force microscopy simulator with phase-locked-loop controlled frequency detection and excitation. *Phys. Rev. B*, 74:235439, 2006.

[63] U. Dürig. Interaction sensing in dynamic force microscopy. *New J. Phys.*, 2:5, 2000.

[64] A. Raman, J. Melcher, and R. Tung. Cantilever dynamics in atomic force microscopy. *Nano today*, 3:20, 2008.

[65] O. Sahin and A. Alatar. Simulation of higher harmonics generation in tapping-mode atomic force microscopy. *Appl. Phys. Lett.*, 79:4455, 2001.

[66] M. Balantekin and A. Atalar. Power dissipation analysis in tapping-mode atomic force microscopy. *Phys. Rev. B*, 67:193404, 2003.

[67] S. Hembacher, F. J. Giessibl, and J. Mannhart. Force microscopy with light-atom probes. *Science*, 305:380, 2004.

[68] A. Sebastian, M. V. Salapaka, D. J. Chen, and J. P. Cleveland. Harmonic analysis based modeling of tapping mode afm. In *Proceedings of the American Control Conference*, volume 1, pages 232–236, San Diego, USA, June 1999.

[69] S. Hu, S. Howell, A. Raman, R. Reifenberger, and M. Franchek. Frequency domain identification of tip-sample van der waals interactions in resonant atomic force microcantilevers. *J. Vib. Acoust.*, 126:343, 2004.

[70] J. Schiener, S. Witt, M. Stark, and R. Guckenberger. Stabilized atomic force microscopy imaging in liquids using second harmonic of cantilever motion for setpoint control. *Rev. Sci. Instrum.*, 75:2564, 2004.

[71] R. D. Turner, J. Kirkham, D. Devine, and N. H. Thomson. Second harmonic atomic force microscopy of living staphylococcus aureus bacteria. *Appl. Phys. Lett.*, 94:043901, 2009.

[72] A. H. Nayfeh and B. Balachandran. *Applied Nonlinear Dynamics: Analytical, Computational and Experimental Methods*. Wiley-VCH, 1995.

[73] O. Sahin, A. Alatar, C. F. Quate, and O. Solgaard. Resonant harmonic response in tapping-mode atomic force microscopy. *Phys. Rev. B*, 69:165416, 2004.

[74] J. W. Li, J. P. Cleveland, and R. Proksch. Bimodal magnetic force microscopy: Separation of short and long range forces. *Appl. Phys. Lett.*, 94:163118, 2009.

[75] W. Han, S.M. Lindsay, and T. Jing. A magnetically driven oscillating probe microscope for operation in liquids. *Appl. Phys. Lett.*, 69:4111, 1996.

[76] X. Xu and A. Raman. Comparative dynamics of magnetically, acoustically, and brownian motion driven microcantilevers in liquid. *J. Appl. Phys.*, 102:034303, 2007.

[77] J. Tamayo and R. Garcia. Relationship between phase shift and energy dissipation in tapping-mode scanning force microscopy. *Appl. Phys. Lett.*, 73(20):2926, 1998.

[78] A. San Paulo and R. Garcia. Tip-surface forces, amplitude, and energy dissipation in amplitude-modulation (tapping mode) force microscopy. *Phys. Rev. B*, 64:193411, 2001.

[79] R. Fürth, editor. *Investigations on the Theory of the Brownian Movement*. Dover Publications, 1956.

[80] P. Mörters and Y. Peres, editors. *Brownian motiont*. Cambridge University Press, 2010.

[81] F. Gittes and C. F. Schmidt. Thermal noise limitations on micromechanical experiments. *Eur. Biophys. J.*, 27:75, 1998.

[82] S. Rast, C. Wattinger, U. Gysin, and E. Meyer. The noise of cantilevers. *Nanotechnology*, 11:169, 2000.

[83] P. R. Saulson. Thermal noise in mechanical experiments. *Phys. Rev. D*, 42:2437, 1990.

[84] D. S. Lemons and A. Gythiel. Paul langevin's 1908 paper "on the theory of brownian motion". *Am. J. Phys.*, 65:1079, 1997.

[85] L. E. Reichl. *A Modern Course in Statistical Physics*. University of Texas Press, 1987.

[86] R. Levy and M. Maaloum. Measuring the spring constant of atomic force microscope cantilevers thermal fluctuations and other methods. *Nanotechnology*, 13:33, 2002.

[87] P. Paolino and L. Bellon. Frequency dependence of viscous and viscoelastic dissipation in coated micro-cantilevers from noise measurement. *Nanotechnology*, 20:405705, 2009.

[88] J. Lübbe, M. Temmen, P. Rahe, A. Kühnle, and M. Reichling. Determining cantilever stiffness from thermal noise. *Beilstein J. Nanotechnol.*, 4:227, 2013.

[89] H. Nyquist. Thermal agitation of electric charge in conductors. *Phys. Rev.*, 32:110, 1928.

[90] J. B. Johnson. Thermal agitation of electricity in conductors. *Phys. Rev.*, 32:97, 1928.

[91] K. Dill and S. Bromberg. *Molecular Driving Forces: Statistical Thermodynamics in Biology, Chemistry, Physics, and Nanoscience*. Garland science, 2010.

[92] T. E. Schäffer. Calculation of thermal noise in an atomic force microscope with a finite optical spot size. *Nanotechnology*, 16:664, 2005.

[93] H.B. Callen and T.A. Welton. Irreversibility and generalized noise. *Phys. Rev.*, 83:34, 1951.

[94] *Introduction to Modern Statistical Mechanics*. Oxford University Press, 1987.

[95] U. M. B. Marconi, A. Puglisi, L. Rondoni, and A. Vulpiani. Fluctuation–dissipation: Response theory in statistical physics. *Phys. Rep.*, 461:111, 2008.

[96] P. Vairac and B. Cretin. Electromechanical resonator in scanning microdeformation microscopy: theory and experiment. *Opt. Commun.*, 132:19, 1996.

[97] M. Shusteff, T. P. Burg, and S. R. Manalis. Measuring Boltzmann's constant with a low-cost atomic force microscope: an undergraduate experiment. *Am. J. Phys.*, 74:873, 2006.

[98] M. Luna, J. Colchero, and A. M. Baro. Study of water droplets and films on graphite by noncontact scanning force microscopy. *J. Phys. Chem. B*, 103:9576, 1999.

[99] M. R. Paul and M. C. Cross. Stochastic dynamics of nanoscale mechanical oscillators immersed in a viscous fluid. *Phys. Rev. Lett.*, 92:235501, 2004.

[100] A. L. Weisenhom, P. Maivald, H. J. Butt, and P. K. Hansma. Measuring adhesion, attraction, and repulsion between surfaces in liguids with an atomic-force microscope. *Phys. Rev. B Condens. Matter.*, 45:11226, 1992.

[101] H. Goldstein. *Classical Mechanics*. Addison Wesley, 1980.

[102] U. Rabe, K. Janser, and W. Arnold. Vibrations of free and surface-coupled atomic force microscope cantilevers: theory and experiment. *Rev. Sci. Instrum.*, 67:3281, 1996.

[103] J. L. Hutter and J. Bechhoefer. Calibration of atomic-force microscope tips. *Rev. Sci. Instrum.*, 64:1868, 1993.

[104] M. A. Lantz, H. J. Hug, R. Hoffmann, P. J. A. van Schendel, P. Kappenberger, S. Martin, A. Baratoff, and H. J. Güntherodt. Quantitative measurement of short-range chemical bonding forces. *Science*, 291:2580, 2001.

[105] S. Kawai, T. Glatzel, S. Koch, A. Baratoff, and E. Meyer. Interaction-induced atomic displacements revealed by drift-corrected dynamic force spectroscopy. *Phys. Rev. B*, 83:035421, 2011.

[106] J. Welker, E. Illek, and F. J. Giessibl. Analysis of force-deconvolution methods in frequency-modulation atomic force microscopy. *Nanotechnology*, 3:238, 2012.

[107] J. P. Cleveland, S. Manne, D. Bocek, and P. K. Hansma. A nondestructive method for determining the spring constant of cantilevers for scanning force microscopy. *Rev. Sci. Instrum.*, 64:403, 1993.

[108] J. P. Cleveland, S. Manne, D. Bocek, and P. K. Hansma. Short cantilevers for atomic force microscopy. *Rev. Sci. Instrum.*, 67:3583, 1996.

[109] J. W. M. Chon, P. Mulvaney, and J. E. Sader. Experimental validation of theoretical models for the frequency response of atomic force microscope cantilever beams immersed in fluids. *J. Appl. Phys.*, 87:3978, 2000.

[110] J. W. M. Chon, P. Mulvaney, and J. E. Sader. Thermomechanical noise of a free v-shaped cantilever for atomic-force microscopy. *Ultramicroscopy*, 86:207, 2001.

[111] S. M. Cook, T. E. Schäffer, K. M. Chynoweth, M. Wigton, R. W. Simmonds, and K. M. Lang. Practical implementation of dynamic methods for measuring atomic force microscope cantilever spring constants. *Nanotechnology*, 17:2135, 2006.

[112] J. P. Cleveland, T. E. Schäffer, and P. K. Hansma. Probing oscillatory hydration potentials using thermal-mechanical noise in an atomic-force microscope. *Phys. Rev. B*, 52:R8692, 1995.

[113] W. F. Heinz, M. D. Antonik, and J. H. Hoh. Reconstructing local interaction potentials from perturbations to the thermally driven motion of an atomic force microscope cantilever. *J. Phys. Chem. B*, 104:622, 2000.

[114] T. Drobek, R. W. Stark, and W. M. Heckl. Determination of shear stiffness based on thermal noise analysis in atomic force microscopy: passive overtone microscopy. *Phys. Rev. B*, 64:045401, 2001.

[115] O. H. Willemsen, M. M. Snel, L. Kuipers, C. G. Figdor, J. Greve, and B. G. D. Grooth. A physical approach to reduce nonspecific adhesion in molecular recognition atomic force microscopy. *Biophys. J.*, 76:716, 1999.

[116] P. Maivald, H. J. Butt, S. A. C. Gould, C. B. Prater, B. Drake, J. A. Gurley, V. B. Elings, and P. K. Hansma. Using force modulation to image surface elasticities with the atomic force microscope. *Nanotechnology*, 2:103, 1991.

[117] M. Radmacher, R. W. Tillamnn, M. Fritz, and H. E. Gaub. From molecules to cells: imaging soft samples with the atomic force microscope. *Science*, 257:1900, 1992.

[118] M. Radmacher, R. W. Tillamnn, and H. E. Gaub. Imaging viscoelasticity by force modulation with the atomic force microscope. *Biophys. J.*, 64:735, 1993.

[119] T. Kajiyama, K. Tanaka, I. Ohki, S. R. Ge, J. S. Yoon, and A. Takahara. Imaging of dynamic viscoelastic properties of a phase-separated polymer surface by forced oscillation atomic force microscopy. *Macromolecules*, 27:7932, 1994.

[120] B. Cappella and G. Dietler. Force-distence curves by atomic force microscopy. *Surf. Sci. Reports*, 34:1, 1999.

[121] S. G. Mallat. *A Wavelet Tour of Signal Processing*. Academic Press, 1999.

[122] C. K. Chui. *An introduction to wavelets*. Academic Press New York, 1992.

[123] P. S. Addison. *The Illustrated Wavelet Transform Handbook*. Taylor and Francis, 2002.

[124] W. Heisenberg. *The Physical Principles of the Quantum Theory*. The University of Chicago Press, 1930.

[125] G. Malegori and G. Ferrini. Tip-sample interactions on graphite studied using the wavelet transform. *Beilstein J. Nanotechnol.*, 1:172, 2010.

[126] Y. Deng, C. Wang, L. Chai, and Z. Zhang. Determination of Gabor wavelet shaping factor for accurate phase retrieval with wavelet-transform. *Appl. Phys. B*, 81:1107, 2005.

[127] S. W. Smith. *The Scientist and Engineer's Guide to Digital Signal Processing*. California Technical Publishing, 1999.

[128] M. Born and E. Wolf. *Principles of Optics*. Cambridge University Press, Cambridge, seventh edition, 1999.

[129] C. Torrence and G. P. Compo. A practical guide to wavelet analysis. *Bull. Am. Meteorol. Soc.*, 79:61, 1998.

[130] A. Grinsted, J. C. Moore, and S. Jevrejeva. Application of the cross wavelet transform and wavelet coherence to geophysical time series. *Nonlinear Proc. Geophys.*, 11:561, 2004.

[131] G. Malegori and G. Ferrini. Wavelet transforms to probe long- and short-range forces by thermally excited dynamic force spectroscopy. *Nanotechnology*, 22:195702, 2011.

[132] J. E. Sader. Calibration of rectangular atomic force microscope cantilevers. *Rev. Sci. Instrum.*, 70:3967, 1999.

[133] J. L. Hutter. Comment on tilt of atomic force microscope cantilevers: Effect on spring constant and adhesion measurements. *Langmuir*, 21:2630, 2005.

[134] H. J. Butt, B. Cappella, and M. Kappl. Force measurements with the atomic force microscope: Technique, interpretation and applications. *Surf. Sci. Reports*, 59:1, 2005.

[135] B. Cappella, P. Baschieri, C. Frediani, P. Miccoli, and C. Ascoli. Force-distance curves by afm: a powerful technique for studying surface interactions. *IEEE Eng. Med. Biol.*, 16:58, 1997.

[136] R. W. Stark, G. Schitter, M. Stark, R. Guckenberger, and A. Stemmer. State-space model of freely vibrating and surface-coupled cantilever dynamics in atomic force microscopy. *Phys. Rev. B*, 69:085412, 2004.

[137] J. Melcher, S. Hu, and A. Raman. Equivalent point-mass models of continuous atomic force microscope probes. *Appl. Phys. Lett.*, 91:053101, 2007.

[138] J. Colchero, A. Storch, M. Luna, J. G. Herrero, and A. M. Baro. Observation of liquid neck formation with scanning force microscopy techniques. *Langmuir*, 14:2230, 1998.

[139] A. L. Weisenhorn, P. Maivald, H. J. Butt, and P. K. Hansma. Measuring adhesion, attraction, and repulsion between surfaces in liquids with an atomic-force microscope. *Phys. Rev. B*, 45:11226, 1992.

[140] T. Eastman and D. M. Zhu. Adhesion forces between surface-modified afm tips and a mica surface. *Langmuir*, 12:2859, 1996.

[141] D. O. Koralek, W. F. Heintz, M. D. Antonik, A. Baik, and J. H. Hoh. Probing deep interaction potentials with white-noise-driven atomic force microscope cantilevers. *Appl. Phys. Lett.*, 76:2952, 2000.

[142] D. Nardi, M. Travagliati, M. E. Siemens, Q. Li, M. M. Murnane, H. C. Kapteyn, G. Ferrini, F. Parmigiani, and F. Banfi. Probing thermomechanics at the nanoscale: Impulsively excited pseudosurface acoustic waves in hypersonic phononic crystals. *Nano Lett.*, 11:4126, 2011.

[143] D. Nardi, E. Zagato, G. Ferrini, C. Giannetti, and F. Banfi. Design of a surface acoustic wave mass sensor in the 100 ghz range. *Appl. Phys. Lett.*, 100:253106, 2012.

[144] E. Cavaliere, G. Ferrini, P. Pingue, and L. Gavioli. Fractal tio2 nanostructures by nonthermal laser ablation at ambient pressure. *J. Phys. Chem. C*, 117(44):23305, 2013.

[145] J.L. Arlett, E.B. Myers, and M.L. Roukes. Comparative advantages of mechanical biosensors. *Nature Nanotech.*, 6:203, 2011.

[146] B. Bhushan, editor. *Handbook of Nanotechnology*. Springer-Verlag Berlin Heidelberg, 2010.

[147] J. R. Lozano, D. Kiracofe, J. Melcher, R. Garcia, and A. Raman. Calibration of higher eigenmode spring constants of atomic force microscope cantilevers. *Nanotechnology*, 21:465502, 2010.

[148] J. Legleiter, M. Park, B. Cusick, and T. Kowalewski. Scanning probe acceleration microscopy (spam) in fluids: Mapping mechanical properties of surfaces at the nanoscale. *Proc. Natl. Acad. Sci. USA*, 103(13):4813, 2006.

[149] G. Malegori and G. Ferrini. Tip-sample interactions on graphite studied in the thermal oscillation regime. *J. Vac. Sci. Technol. B*, 28:C4B18, 2010.

[150] J. P. Cleveland, B. Anczykowski, A. E. Schmid, and V. B. Elings. Energy dissipation in tapping-mode atomic force microscopy. *Appl. Phys. Lett.*, 72(20):2613, 1998.

[151] R. Garcia, C. J. Gomez, N. F. Martinez, S. Patil, C. Dietz, and R. Magerle. Identification of nanoscale dissipation processes by dynamic atomic force microscopy. *Phys. Rev. Lett.*, 97:016103, 2006.

[152] C. Gackenheimer, L. Cayon, and R. Reifenberger. Analysis of scanning probe microscope images using wavelets. *Ultramicroscopy*, 106:389, 2009.

[153] M. Carmichael, R. Vidu, A. Maksumov, A. Palazoglu, and P. Stroeve. Using wavelets to analyze afm images of thin films surface: micelles and supported lipid bilayers. *Langmuir*, 20:11557, 2004.

[154] K. Yamanaka and S. Nakano. Quantitative elasticity evaluation by contact resonance in an atomic force microscope. *Appl. Phys. A*, 66:S313, 1998.

[155] V. Pukhova and G. Ferrini. Study of transitory regimes of thermally excited cantilevers by using the wavelet transform. In *Modern Engineering and Technologies of the Future: International scientific online conference*, volume 1, pages 90–96, Krasnoyarsk Territory, Russia, February 2013.

[156] F. Banfi and G. Ferrini. Wavelet cross-correlation and phase analysis of a free cantilever subjected to band excitation. *Beilstein J. Nanotechnol.*, 3:294, 2012.

Acknowledgments

I would like to express my special appreciation and gratitude to my advisor, Prof. Gabriele Ferrini, who introduced me to Atomic Force Microscopy and wavelet transform. You have been a great mentor for me with your tremendous passion, creativity and generosity. I would like to thank you for giving me a freedom in defining my research aims and methods, encouraging and supporting me at every step of the way, and for allowing me to grow as a scientist. Your advices on both research and career are priceless.

I would like to acknowledge Prof. Santiago Solares for having kindly accepted to act as referee of the present thesis and for his accurate comments.

I would also like to thank my committee members, Prof. Giulio Cerullo and Prof. Massimo Capone for their work.

A special thanks goes to Dr. Francesco Banfi, with whom I had the pleasure to collaborate. I am very thankful to Dr. Luca Gavioli, who explained to me the working principles of the AFM set-up. I wish to particularly thank Dr. Emanuele Cavaliere for helping me with laboratory facilities, for his technical knowledge and countless explanations. Thank you for being always available and patient with me.

As a PhD student I have been fortunate to receive financial support that allowed me to fully dedicate my time to the present research and to participate in conferences and schools. I am thankful to the Università degli Studi di Milano and Università Cattolica del Sacro Cuore for that. I feel privileged to receive this opportunity.

My PhD study required more than academic support.

I wish to thank my friends in the Department for shared the joys and the difficulties of being a doctoral student, Stefano Ponzoni deserves a special mention. I would like to thank Lucia Bossoni for her friendship and help from the very beginning. A huge thanks goes to Marina Samoylova, who has been unwavering in her personal support during the time I spent at the University. Outside the University I wish to thank Yulia Orlova and Lira Troci with whom I have been fortunate to meet. I must thank everyone above also for many memorable evenings out and for moments we shared together, because of you my staying in Italy was a wonderful experience and this I will never forget.

I would like to thank all of my friends who stayed with me and supported me in writing, and incited me to strive towards my goal. I wish to specially mention Irina Zaitseva, Nadezhda Yufrikova, Elena Ivashchenko, Maria Dikusar and Natalia Gavrichkina, who have been kind and supportive to me. Thank you for listening to and, sometimes, having to tolerate me over the past several years. You have been an uninterrupted source of moral support and your friendship is priceless.

Most importantly, none of this could have happened without my great family. I am very thankful to my Father Mikhail and Mother Tatiana, who always nurture my curiosity and raise my independence, and to my sister Anastasia. As a family, we have experienced some ups and downs in the past years and for all of the sacrifices and support that you have made on my behalf I am forever grateful. I also wish to thank my Grandmother Antonina, who is my greatest inspiration. This thesis is a testament of your unconditional love and encouragement.